Precambrian Research 325 (2019) 192–216

Contents lists available at ScienceDirect

Precambrian Research

journal homepage: www.elsevier.com/locate/precamres

Geochemistry of banded iron formations and their host rocks from the Central Eastern Desert of Egypt: A working genetic model and tectonic implications

A.K. El-Shazly[a,*], K.I. Khalil[b], H.A. Helba[b]

[a] Geology Department, Marshall University, Huntington, WV 25755, United States
[b] Geology Department, University of Alexandria, Faculty of Science, Moharram Bey, Alexandria, Egypt

ARTICLE INFO

Keywords:
Central Eastern Desert of Egypt
Banded iron formation
Thermobarometry
Cathodoluminescence imaging
U-Pb zircon ages
Tectonic evolution

ABSTRACT

Banded iron formations (BIF) occur intercalated with Neoproterozoic volcanosedimentary units in 13 localities in the Egyptian Central Eastern Desert (CED). These units are characterized by magnetite and hematite-rich layers alternating with quartz-rich layers containing andradite–rich garnet, epidote, ± calcite in the southern parts of CED, and chlorite ± stilpnomelane, and calcite in the north. Localized hydrothermal alteration affected most deposits and is manifested by secondary Ca–bearing minerals. All BIFs and their host rocks were strongly deformed and metamorphosed under greenschist to epidote amphibolite facies conditions during the collisional stage of the Pan African orogeny.

Geochemically, CED BIFs have higher Fe/Si compared to Algoma, Superior, or Rapitan BIF types. All BIFs have rare earth element – Y patterns similar to those of modern day oceanic water, with a few samples displaying a weak positive Eu anomaly. All BIFs have high SiO_2/Al_2O_3 and Fe/Ti, and low Al/(Al + Fe + Mn), which suggest a hydrogenous origin with hydrothermal contributions and low detrital component. Geochemical trends, Y/Ho, and Pr/Yb values suggest deposition of Wadi El Dabbah BIF closest to land and Um Nar and Wadi Kareim closest to hydrothermal vents. Host metavolcanic and metavolcaniclastic rocks show chemical signatures indicative of an immature oceanic arc setting with MORB affinities for the southern areas and back- or fore-arc basin affinities for the northern localities.

These results lead to the conclusion that CED BIFs and their host rocks formed in small intra-arc basins and sloped or terraced silled basins in the back- and fore-arc areas surrounding an immature island arc. Restricted circulation of hydrothermal fluids in these basins concomitant with arc volcanism increased Fe^{+2} and Si in solution. During periods of arc quiescence, oxidation of Fe^{2+} led to deposition of Fe-oxyhydroxide. Diagenesis formed fine-grained magnetite, whereas subsequent hydrothermal alteration and metamorphism formed porphyroblastic magnetite and specularite.

1. Introduction

Banded iron formations (BIFs) are widely accepted as products of chemical precipitation of Fe^{2+} and Fe^{3+} oxides and hydroxides, Fe-rich silicates (± carbonates and/or sulfides), and silica in a marine environment, followed by significant diagenetic and metamorphic modifications (e.g. James, 1992; Klein and Beukes, 1993a). Because most BIFs are Archean to Palaeoproterozoic in age (Abbott and Isley, 2001; Huston and Logan, 2004; Klein and Beukes, 1993a), their abundance versus paucity have been used by many authors to constrain the timing of the Great Oxygenation Event (GOE) at *c.* 2.4 Ga (e.g. Garrels et al., 1973; Klein, 2005a,b; Simonson, 2003). The occurrence of a few relatively small-sized BIFs deposited 850–700 Ma (e.g. Ilyin, 2009; Klein and Ladeira, 2004; Yeo, 1986) has therefore been attributed to the global glaciation hypothesis known as Snowball Earth (e.g. Hoffman et al., 1998; Kirschvink, 1992). Other authors attribute the formation of these Neoproterozoic BIFs to specific tectonic and/ or volcanic events (e.g. Basta et al., 2011; Freitas et al., 2011; Eyles and Januszczak,

Abbreviations: ANS, Arabian-Nubian shield; BIF, banded iron formation; BSEI, back scattered electron image; CED, Central Eastern Desert; Fh, ferrihydrite; ga, gahnite; Goe, goethite; hc, hercynite; Hem, hematite; Ilm, ilmenite; jd, jadeite; mg #, Mg/(Mg + Fe); NED, northern Eastern Desert, PPL, plane-polarized light; ps, pistacite, REE, rare earth elements; RL, reflected light, SED, Southern Eastern Desert; sp, spinel; usp, ulvospinel; X_i, mole fraction of component "i"

* Corresponding author at: Geology Department, Marshall University, 1 John Marshall Drive, Huntington, WV 25755, United States.
E-mail address: elshazly@marshall.edu (A.K. El-Shazly).

https://doi.org/10.1016/j.precamres.2019.02.011
Received 7 July 2018; Received in revised form 8 February 2019; Accepted 12 February 2019
Available online 13 February 2019
0301-9268/

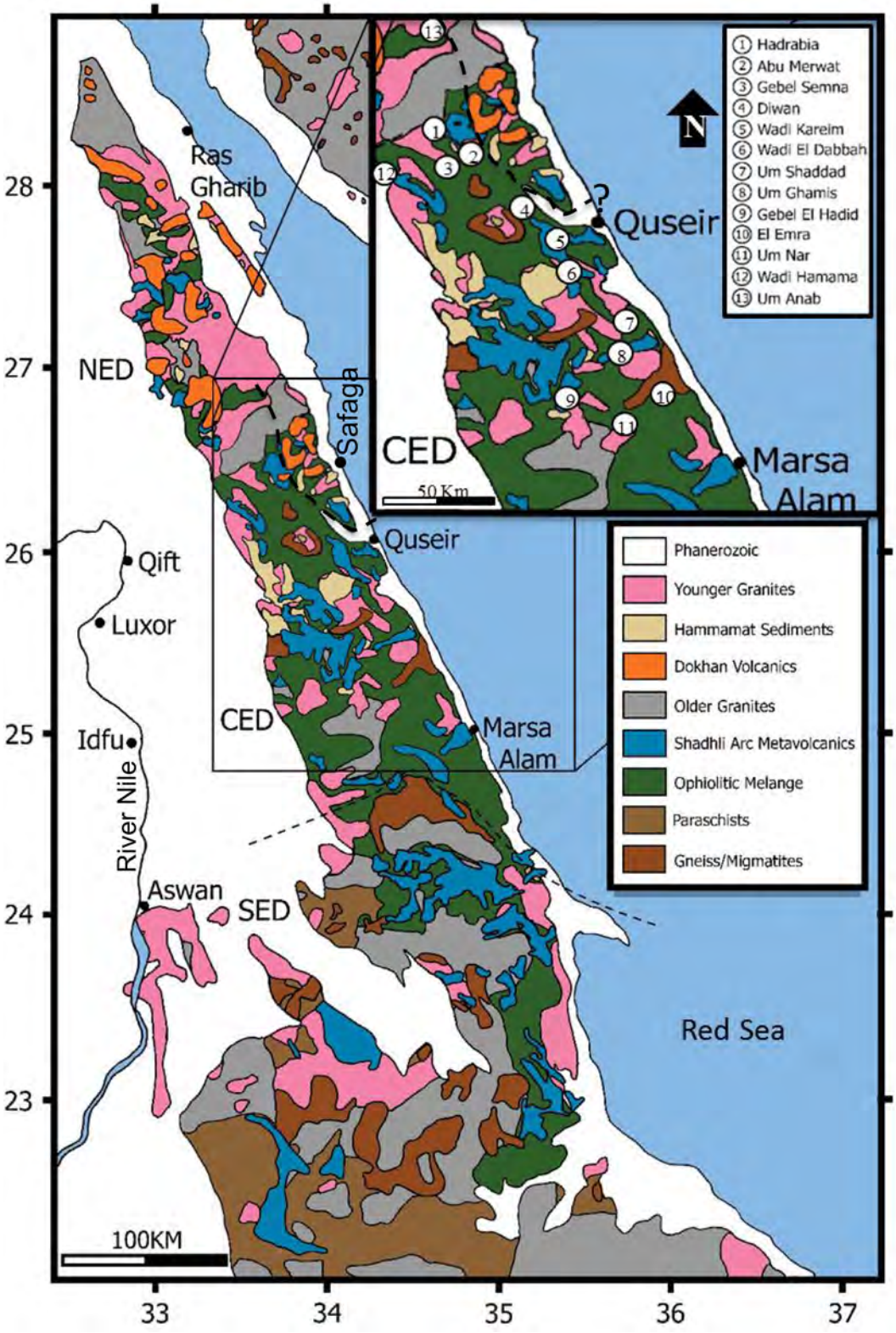

Fig. 1. Simplified lithological map of the Eastern Desert basement in Egypt (compiled from Breitkreuz et al., 2010, Egyptian Geological Survey, 1981, Hassan and Hashad, 1990, and Stern and Hedge, 1985). Dashed lines represent the boundaries between the northern, central and southern parts of the eastern desert (cf. Stern and Hedge, 1985 and text). Inset shows the locations of 13 banded iron-ores (open circles).

2004), or to large igneous provinces/ super plumes, rather than global climatic changes (e.g. Isley, 1995; Isley and Abbott, 1999; Ohmoto et al., 2006). In all cases, the occurrence of BIFs in an area has important paleotectonic and paleoenvironmental implications, making their study essential for any successful tectonic interpretation.

In Egypt, BIFs occur in 13 localities in an area of *c.* 30,000 km^2 in the Central Eastern Desert (CED, Fig. 1). These small deposits have been classified as Algoma type BIF (e.g. Sims and James, 1984), although they occur intercalated with Neoproterozoic volcaniclastic and epiclastic sediments of intermediate composition (e.g. Ali et al., 2009),

rather than the typical Archean/ Paleoproterozoic basic volcanic rocks associated with most Algoma type BIFs (e.g. Bekker et al. 2010; Gross 1996; Klein, 2005a,b). Despite numerous studies on the Egyptian BIFs (cf. Khalil and El-Shazly, 2012 for a review), their origin and evolution are still poorly understood. El Aref et al. (1993) suggested a Superior type origin for the Um Nar BIF (deposit #11; Fig. 1), which they considered to be Archean in age. Salem et al. (1994) concluded that BIF from El Imra (# 10; Fig. 1) formed by contact metasomatism, whereas El Habaak (2004) concluded that some bands of Um Nar BIF represent a skarn formed by mixing hydrothermal and meteoric fluids driven by granitic intrusions. Ali et al. (2010) and Stern et al. (2013) attributed BIF deposition in CED to concomitant melting of glacial ice *c.* 750 Ma, whereas Basta et al. (2011) suggested a volcanogenic origin for BIFs from Wadi Kareim (# 5; Fig. 1) and Um Anab (# 13; Fig. 1). However, none of these models provide an explanation for the restriction of BIFs to the CED, or integrates their origin into the tectonic framework of the Eastern Desert of Egypt.

Based on a field, petrological, and geochronological study of the rocks hosting the BIFs, El-Shazly and Khalil (2016) suggested that BIF precursor minerals were deposited in silled portions of fore- and back-arc basins during periods of volcanic quiescence from an arc active between 860 and 670 Ma. According to this model, BIF deposits south of Wadi El Dabbah (# 6, Fig. 1) formed in the back arc basin, whereas those to the north formed in a fore arc basin. Closure of these basins occurred during the culmination of the Pan African Orogeny 680–640 Ma (Kröner and Stern, 2004), and resulted in the emplacement of ophiolites and associated BIFs onto the arc. Although this model explains why BIFs are restricted to the CED, it contradicts other tectonic models for the area on issues as to the nature of the basin(s) in which the BIFs developed, polarity of subduction, and direction of obduction (e.g. Loizenbauer et al., 2001; Shalaby et al., 2005; Abd El-Rahman et al., 2009; Farahat, 2010).

The aim of this study is to present geochemical data, collected over the course of five years, on the CED BIFs and their host rocks in order to identify and explain: (1) the chemical, mineralogical, and textural differences and similarities amongst the CED BIFs; (2) the source of Fe and Si for these BIFs; and (3) the geochemical signatures of the BIFs and their host rocks. The results of this study will lead to a better understanding of the tectonic setting of the CED and the origin of their BIFs, and will allow us to test some of the hypotheses for their formation (e.g. Ali et al., 2009; Basta et al., 2011; El-Shazly and Khalil, 2016).

2. Geologic setting: field and structural relations

The basement rocks of the Egyptian Eastern Desert consist of (i) 1.8 Ga–680 Ma migmatites and gneisses that constitute several "metamorphic core complexes" (e.g. Hassan and Hashad, 1990; Loizenbauer et al., 2001; Andresen et al., 2007); (ii) 850–700 Ma "ophiolitic mélanges" and coeval "arc assemblages" that include volcaniclastic and volcanic rocks intercalated with epiclastic sedimentary rocks (e.g. El-Gaby et al., 1990); (iii) "Older granitoids" intruded 710–610 Ma (Stern and Hedge, 1985; Moussa et al., 2008) but also as old as 850–800 Ma in some places (Shiatian granite; Hassan and Hashad, 1990); (iv) 630–592 Ma old, medium- to high- K, calcalkalic Dokhan arc volcanic rocks, (e.g. Breitkreuz et al., 2010) and 606–585 Ma old Hammamat molasse type sedimentary rocks (Moussa et al., 2008) that overlie units (i)–(iii); and (v) "Younger granitoids" which intruded all units 620–505 Ma (e.g. Hassan and Hashad, 1990).

Stern and Hedge (1985) subdivided the Eastern Desert into three terranes: northern (NED), central (CED), and southern eastern desert (SED) based on distribution of rock types and their absolute ages (Fig. 1). The NED is characterized by a paucity of serpentinites, abundance of post-orogenic "Younger granitoids", and is the terrane with the most outcrops of Dokhan volcanics. The CED is predominated by ophiolitic mélanges and arc assemblages intercalated in places with banded iron formations. The SED is characterized by the predominance of "Older granitoids" and a relatively high abundance of gneisses and migmatites. This distribution gives rise to a general apparent trend of decreasing age to the north (Stern and Hedge, 1985).

Based on structural elements, and the occurrence of outcrops of Dokhan Volcanics near Safaga and a BIF at Um Anab (# 13, Fig. 1), a new boundary between the CED and NED is herein proposed. This boundary follows a series of distinct shear zones/ lineaments the most prominent of which are the NW-SE trending zone west of Quseir, and a NE-SW trending shear zone separating outcrops of Dokhan Volcanics from ophiolitic rocks near Um Anab (Fig. 1). Accordingly, all BIFs would be restricted to the CED and all medium to high K calcalkalic Dokhan Volcanics to the NED (Fig. 1). The "Allaqi Dokhan Volcanic Suite" rocks in the southernmost extremity of the CED (El-Nisr, 1997; El-Sayed et al., 2004) are described as low to medium K mafic to felsic rocks that do not conform to the criteria of Stern et al. (1984) set for the Dokhan Volcanics.

Structurally, the CED was affected by four distinct deformational events (D1–D4; Fig. 2; Loizenbauer et al., 2001; Shalaby et al., 2005). D1 is pre-Pan-African deformation observed only in amphibolite xenoliths in granitic gneisses. D2 resulted from the closure of inter-arc basins, ophiolite obduction, collision of East and West Gondwana, and regional metamorphism under greenschist to amphibolite facies conditions (e.g. Loizenbauer et al., 2001). In the southern part of the CED, D2 is represented by a series of tight overturned folds that verge to the NE with E–W to NW–SE striking, south–dipping axial planes, as well as E–W striking and south–dipping thrusts. In Wadi El Dabbah (# 6, Fig. 1), D2 is characterized by E–verging tight and overturned folds and thrusts with N–S strikes and dips to the west. D3 is a transpressional event marking the terminal stages of the Pan-African Orogeny (e.g. Loizenbauer et al., 2001). To the south of Wadi El Dabbah, D3 is represented by a series of open folds with NW–SE trending axes. In the northern part of the CED, D3 is characterized by tight, overturned, SW–verging anticlines with NW–SE striking, and NE–dipping axial planes (e.g. Noweir et al., 2004; El-Shazly and Khalil, 2016). D4 deformation is represented by several prominent shear zones and strike slip faults that are considered part of the Najd system (cf. Loizenbauer et al., 2001). Fig. 2 summarizes these relations, and relates structures and igneous and metamorphic events to the tectonic model of El-Shazly and Khalil (2016).

In this study, we present geochemical data collected for eight of the thirteen areas with exposures of BIF. Listed from south to north with numbers in parentheses referring to Fig. 1, these areas are: Um Nar (11), El Imra (10); Gebel El Hadid (9), Um Ghamis (8), Wadi El Dabbah (6), Wadi Kareim (5), Gebel Semna (3), and Abu Marwat (2). Rock units hosting the BIFs in these areas and throughout the CED belong to the "arc assemblage" and "ophiolitic mélange" units, respectively (Fig. 1), and consist of (i) metatuffs to meta-agglomerates, collectively termed "metavolcaniclastics", or (ii) basic to intermediate volcanic to hypabyssal rocks described here as "metavolcanics" (cf. El-Shazly and Khalil, 2016). Both types of host rocks were regionally metamorphosed under greenschist to epidote amphibolite facies conditions, most likely during the Pan-African Orogeny (e.g. Ali et al., 2009; Loizenbauer et al., 2001). According to El-Shazly and Khalil (2014, 2016), metamorphic conditions ranged from 520 ± 30 °C, 5 ± 2 kbar in Um Nar in the southern part of the CED to 400 ± 50 °C, 4 ± 2 kbar in the northern areas of Wadi Kareim and Abu Marwat.

The BIFs are interlayered with the metavolcaniclastics (Fig. 3a & b), where they occur as relatively small tabular bodies with strikes that range from tens of meters to 4 km. The thickness of individual layers ranges from a few centimeters to 15 m but rarely exceeds 5 m. Following the classification of Beukes and Gutzmer (2008), most CED BIFs are femicrites with a streaky or continuous rhythmic banding defined by iron oxide rich layers alternating with jaspilites or silicate laminae (Fig. 3c and d). Lithic fragments in BIF layers are rare in most deposits (e.g. Um Nar, Gebel El Hadid and Um Ghamis) but quite common in Wadi El Dabbah, where they display vesicular, amygdaloidal, eutaxitic,

Age (Ma)	Continent/ Arc SED	Inter-Arc Basin CED	Continent/ Arc CED & NED			Deformati-on/ Other
<570			Younger Granite			
606 — 585			Contact metam-orphism	Hammamat		D4b: Najd system: sinistral
620 — 580						D4a: Najd system: dextral
614 — 590			Pan-African Orogeny	Partial exhumation of core complexes	Dokhan Volcanism	D3: transpression/ lateral extrusion ; N and S directed thrusting
640 – 616				Regional metamorph-ism Older Syntectonic Granites and Gabbros		Island arc accretion
680 – 640				Obduction, accretion, and basin closure		D2: N-directed thrusting and folding
690 – 670			Older granite (El-Imra)			
850 — 700	Younger (Shadhli) metavolcanics Shiatian granitoids?	Volcaniclastic debris **Banded Iron Formation (BIF)** Oceanic crust: Older metavolcanics	Arc volcanism: Younger (Shadhli metavolcanics) Migmatites			D1: isoclinal folds in amphibolite xenoliths in core complexes
1800 — 850			Migmatites			

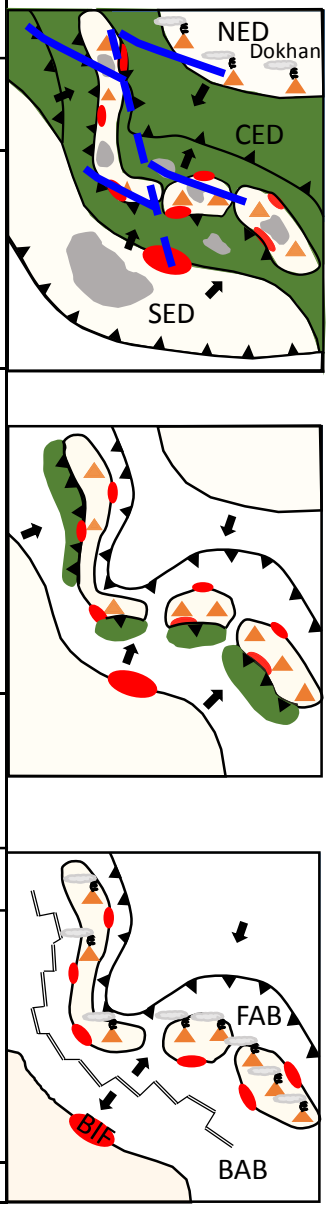

Fig. 2. Stratigraphic and lithotectonic units of the Egyptian Eastern Desert related in space and time to the deformational events identified by Loizenbauer et al. (2001) and Shalaby et al. (2005). Inset frames to the right: map views of CED depicting its tectonic evolution. Legend: BAB: back arc basin; FAB: fore arc basin; red: BIF, green: ophiolitic mélange ± island arc related metavolcaniclastics; grey: "Older Granites". Age constraints are from Stern and Hedge (1985), Hassan and Hashad (1990), Loizenbauer et al. (2001), and Breitkreuz et al. (2010). (For interpretation of the references to colour in this figure legend, the reader is referred to the web version of this article.)

and porphyritic textures (Hamimi, 1988; Takla et al., 1999; Khalil and El-Shazly, 2012). On the other hand, the deposits of Hadrabia (Essawy et al., 1997), and Abu Marwat (1 and 2, Fig. 1) are characterized by layers with a distinct pisolitic texture (Fig. 3e–g). All deposits show some evidence of localized hydrothermal alteration manifested by veins of calcite and other Ca–rich minerals, and/ or a characteristic porous texture (e.g. W. Kareim; Fig. 3h). Weathering variably affects most deposits, and under extreme circumstances forms red and yellow ochers (e.g. Gebel Semna).

3. Analytical techniques

A total of 132 samples were analyzed over the course of five years for major ± trace and RE elements after pulverization in WC mills. Fifty-seven of these samples are BIFs, the main focus of this study. The remaining samples represent 50 metavolcaniclastics, 11 metavolcanics, and 14 felsic intrusions. Major and trace element analysis for all samples from Gebel El Hadid (Khalil et al., 2015), 5 BIFs from Um Ghamis, and 2 from Abu Marwat, was carried out at Acme Analytical

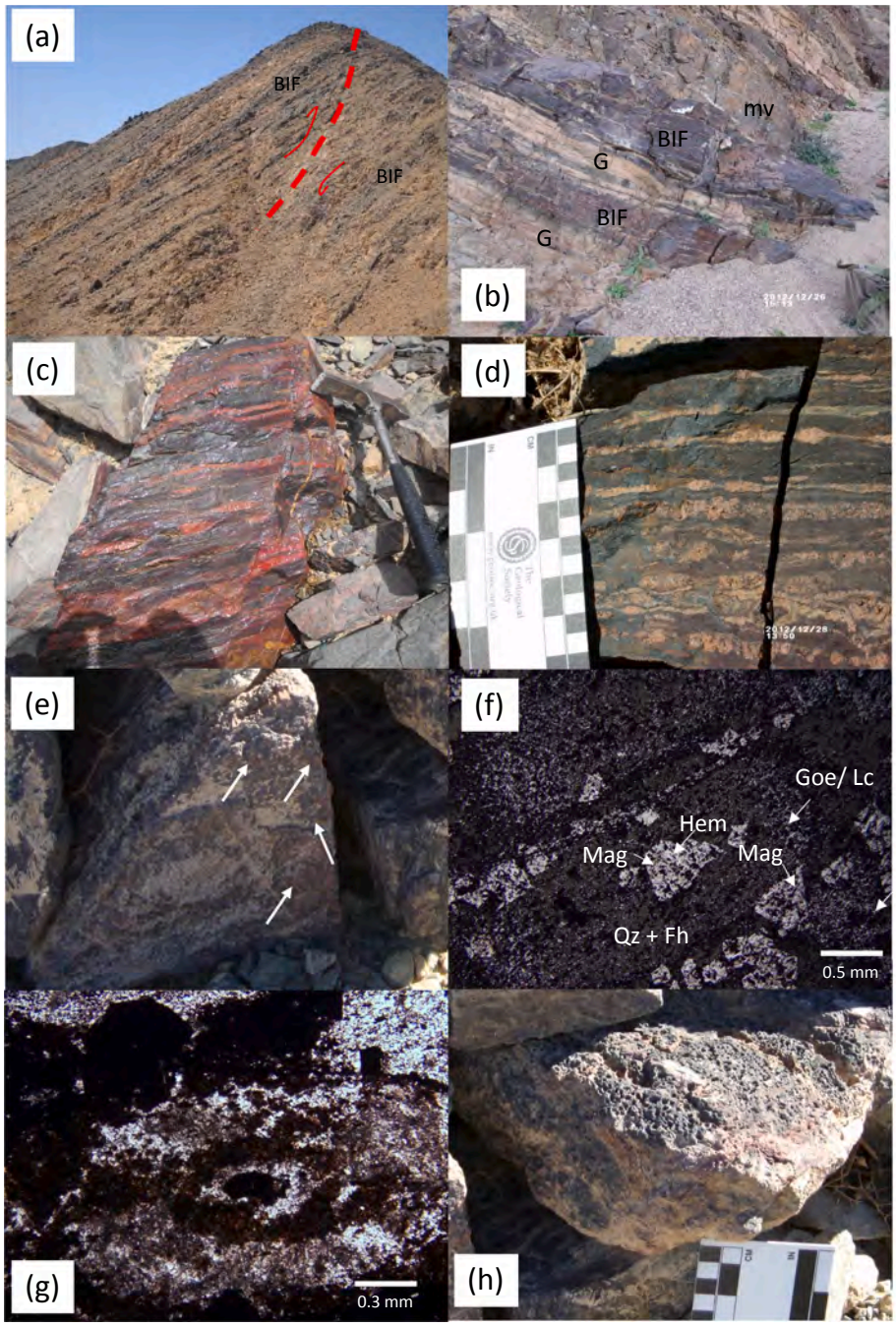

Fig. 3. (a) Folded and faulted BIF intercalated with metavolcaniclastics, Um Nar, looking North; (b) 20–30 cm thick bands of iron ore intercalated with metavolcaniclastics (mv), and intruded by granitic sills (G); El Imra, view looking S65°E; (c) Continuous and streaky rhythmic banding in BIF defined by bands of iron ore alternating with jaspilites; Wadi Kareim; (d) Streaky rhythmic banding in BIF defined by bands of iron oxides alternating with silicate rich bands with garnet; Um Nar; (e) Granular BIF sample with reddish pisolites (arrows); average radius ~0.35 cm; Abu Marwat; (f) Photomicrograph of two pisolites, MW-11, Abu Marwat; reflected light. Note the partially martitized crystals of magnetite (Mag) in the core of one of the pisolites. Pisolites consist of quartz with dusty hematite/ferrihydrite? (Fh) + goethite (Goe)/lepidocrocite (Lc) + flakes of chlorite; (g) Another pisolite from MW-11 viewed under transmitted plane polarized light; (h) example of a porous texture exhibited by altered BIF samples; Abu Marwat.

laboratories, Canada with methods LF-100/ LF-200/ AQ 200. These two methods utilize ICP - MS techniques following sample fusion with lithium metaborate/ tetraborate and nitric acid digestion (for high field strength element analysis), or Aqua Regia digestion for base metal determination.

All other samples were prepared and analyzed at Marshall University and/ or at ALS Minerals, Reno, NV. For major element analysis at Marshall University, the lithium metaborate/ tetraborate flux fusion/ dissolution in 1:7 H_2SO_4 "single solution" method was implemented (e.g. Suhr and Ingamells, 1966; Ingamells, 1966; Shapiro, 1975). Calibration was carried out using one of well - characterized standards SCH-1, FER-4, AGV-1, GSP-1, W-2, or G-2, carefully selected depending on type of rock analyzed, and diluted to obtain a suitable four–point calibration curve. FeO weight % was determined at ALS Minerals by titration with $K_2Cr_2O_7$ after acid digestion with H_2SO_4 and HF (method Fe-VOL05), or by spectrophotometry at Marshall University after digestion with H_2SO_4 + HF in the presence of o-phenanthroline (Fritz and Popp, 1985). Loss on ignition (LOI) calculations were carried out at Marshall University after heating all powders to 1050 °C in a muffle furnace for one hour.

For the analysis of the trace elements Ba, Sr, Rb, La, Ce, Nb, Y, and Zr, the samples were prepared by fusion of 0.2 g of rock powders with lithium metaborate/ tetraborate in graphite crucibles and dissolution in reagent grade 5% HCl (e.g. Cremer and Schlocker, 1976; Delijska et al., 1988). For the analysis of Cu, Co, Zn, Ni, Sc, Cr, and V, sample powders were dissolved in PTFE beakers with HNO_3 and HF overnight, dried, and the residue dissolved in reagent grade HCl (acid digestion technique; e.g. Briggs, 2002). Analysis of USGS standards AGV-1, GSP-1, W-2, BHVO-1, STM-1, SDC-1, and G-2, followed by linear regression after elimination of outliers, allowed us to generate a calibration curve with a minimum of three points for each trace element and a goodness of fit coefficient (R^2) of 0.8 or better. We prefer this technique over the

dilution of elemental standard aqueous solutions as it overcomes the matrix effect problems in spectrochemical analysis. All analyses at Marshall University were carried out using a radial view Liberty 110 ICP-AES from Varian Inc. (2012–2016), or a dual view Agilent 5110 DV ICP-AES (2017).

In addition, 46 BIF samples and 22 host rocks were analyzed for trace elements at ALS Minerals, Nevada, using methods ME-ICP61 (for Cu, Co, Zn, Ni, Sc, Cr, and V) and ME-MS81 (for Ba, Sr, Rb, Nb, Y, Zr, and REE). Sample preparation for these two methods are equivalent to the methods described above, with the base metals analyzed using an ICP-AES (ME-ICP61), and the high field strength elements analyzed by ICP-MS (ME-MS81). To ensure interlab consistency, nine samples were analyzed for trace elements at all three labs. Analyses for most elements are reproducible within 5% (20% for a few elements) at all three labs.

Precision (% relative standard deviation) for major, trace, and rare earth elements is estimated at 1% or better (usually < 0.6%), 1–2%, and < 3%, respectively. Accuracy (calculated by routinely analyzing standards as unknowns at Marshall University) is considered to be 2% or better for major elements, and 10% or better for most trace elements. Detection limits are: 20 ppm for Ni, 10 ppm for Cr; 5 ppm for V; 2 ppm for Zr; 1 ppm for Sc, Ba, and Zn; 0.5 ppm for Sr, Ce and La; 0.3 ppm for Nd; 0.2 ppm for Co, Hf and Nb; 0.1 ppm for Y and Cu, 0.01 ppm for Lu and Tm, 0.02 ppm for Pr, Eu, and Ho; 0.03 ppm for Er; and 0.05 ppm for Th, Sm, Gd, Dy, and Yb.

4. Petrology and mineral Chemistry

4.1. Banded iron formations

All thirteen deposits are characterized by oxide–rich bands intercalated on a millimeter scale with silicate ± carbonate – rich ones. Sulfide rich bands consisting of pyrite (~50%) + magnetite ± pyrrhotite ± chalcopyrite ± sphalerite occur only in Gebel El Hadid (Hamimi, 1988). The oxide bands are predominated by magnetite and hematite, each comprising 10–80% by volume (Table 1). The relative abundance of these two minerals varies from one deposit to another and even from layer to layer in the same deposit. Quartz constitutes 5 to 30% of BIFs where it occurs as an interstitial phase, but is nearly lacking from the highly altered samples (e,g. Gebel Semna ochers). Quartz also occurs in thin anastomosing veinlets that crosscut banding. Chlorite, goethite, and lepidocrocite occur in minor amounts (< 10%), although the latter two minerals constitute up to 30% of weathered femicrites, or the granular BIFs (Fig. 3f, g).

Silicate-rich bands range from jaspilites consisting of microcrystalline quartz with inclusions of extremely fine–grained iron oxide/ hydroxide (ferrihydrite?; giving rise to the texture referred to as “salt and pepper” or “dusty hematite”; e.g. Beukes and Gutzmer, 2008), to quartz–rich bands that include some or all of the minerals: magnetite, hematite, garnet, epidote, and calcite (Fig. 4a). Minor amounts of one or more of the minerals actinolite, diopside, plagioclase feldspar, chlorite, stilpnomelane, and apatite occur in a few samples (Table 1). Garnet is restricted to four deposits: Um Nar, El Imra, and Um Ghamis in the south (characterized by higher metamorphic grade), where it constitutes up to 25% of the mode of some silicate bands (Takla et al., 1999; El-Shazly and Khalil, 2014), and Wadi El Dabbah, where it is a rare mineral restricted to fracture – filling veins of quartz and epidote (El-Shazly and Khalil, 2016). On the other hand, stilpnomelane is restricted to the northern deposits of Wadi Kareim and Hadrabia, whereas greenalite was reported only in Hadrabia (Essawy et al., 1997).

The carbonate bands consist of the same minerals occurring in the silicate bands embedded in a matrix of calcite (with some ankerite and siderite). Like quartz, calcite also occurs in an intricate network of anastomosing veins and veinlets lined by minor amounts of Fe-rich chlorite and goethite. In general, deposits occurring to the north of Wadi El Dabbah are characterized by a higher abundance of carbonate bands and veins.

Texturally, the oxide bands are characterized by three generations of magnetite: (i) very fine-grained (< 40 μm) euhedral crystals clustered in chain-like aggregates or disseminated in microcrystalline quartz (Mag I; Fig. 4b); (ii) coarser-grained (≤125 μm) euhedral to subhedral crystals (Mag II) with sieve textures and/ or patchy to rare oscillatory-like zoning (Fig. 4c–f); and (iii) medium-grained (≤500 μm) anhedral to subhedral porphyroblasts (Mag III; Fig. 4g). Magnetite varieties I and II are only partially altered to hematite along their rims (e.g. Fig. 4f), whereas magnetite III, which is almost always restricted to the southern deposits, can be completely martitized. Compositionally, all three textural varieties of magnetite are very similar, and characterized by Si < 0.05 apfu, Xusp < 0.005, and Xhc < 0.02 (Supplementary Table 1). Darker tones on back scattered electron images of those magnetite II crystals with patchy or oscillatory zoning are characterized by a higher Xhc (usually 0.02), and a greater Y site deficit in contrast to the corresponding brighter areas in which Xmag > 0.99 and Y site occupancy ≥ 1.95 (Supplementary Table 2).

Textural varieties of hematite include (i) fine-grained (≤15 μm) acicular crystals oriented with the banding in quartz-rich bands or concentrated in clusters alternating with magnetite-rich bands (Fig. 4a); (ii) coarser-grained crystals pseudomorphing magnetite II (Fig. 4h); and (iii) coarse-grained (up to 500 μm) platy crystals (specularite). The latter variety is characteristic of Um Nar and occurs in apparent textural equilibrium with magnetite III (Fig. 4i; El-Shazly and Khalil, 2014). All analyzed crystals of hematite are homogeneous with Xhem = 0.95–0.98 and Xilm < 0.02. The only exception is a dense cluster of acicular crystals from Wadi El-Dabbah in which Xilm = 0.035–0.045 (DB-144; Supplementary Table 2). Goethite forms along the rims of hematite (Fig. 4h) and concentrates in bands or voids between magnetite and hematite crystals giving rise to a colloform texture in some porous samples (Fig. 4j). In granular BIFs, goethite (with lepidocrocite and chlorite) occur in layers that surround partially martitized magnetite surrounded by layers of dusty quartz (Fig. 3f and g).

Garnet occurs in millimeter– to centimeter– wide bands that alternate with epidote, quartz, and Fe-oxide rich bands in Um Nar, El Imra, and Um Ghamis (Fig. 4a), or in veins in Wadi El Dabbah. Garnet crystals occur as sizeable (0.7–1 mm), euhedral to anhedral porphyroblasts with inclusions of epidote, quartz, amphibole, magnetite, and hematite. Many crystals are elongated parallel to the banding. Compositionally, these garnets are andradite–grossular solid solutions with Xadr = 0.62–0.95, Xgrs = 0–0.35, Xalm < 0.09. Most crystals are either unzoned, or display a weak patchy zoning pattern (El-Shazly and Khalil, 2014).

Epidote occurs as coarse-grained poikiloblasts with inclusions of quartz, magnetite and hematite that concentrate in bands typically separating garnet and magnetite + quartz - rich bands from the dense oxide – rich ones in Um Nar, El Imra, and Um Ghamis (e.g. Fig. 4a). In Wadi El Dabbah, epidote occurs as fine-grained granular crystals randomly disseminated in the silicate bands or in veins. Compositionally, all epidote is Fe-rich with Xps = 0.21–0.37. Epidote does not occur in BIFs from Gebel El Hadid, Wadi Kareim, Gebel Semna, or Abu Marwat.

Actinolite (Mg # = 0.75–0.95, Al^{iv} < 0.8, Na^{M4} < 0.14, and A site occupancy of < 0.4) is a minor phase in Um Nar, occurring as fibrous inclusions in garnet, rimming pyroxene and garnet, or intergrown with epidote and hematite. Diopside (quadrilateral component of 0.87–0.94, X_{jd} < 0.22, and Mg # = 0.72–0.81) is also restricted to Um Nar where it occurs as fine-grained crystals rimmed by fibrous actinolite, and surrounded by epidote and magnetite (El-Shazly and Khalil, 2014). Chlorite is a rare, minor secondary phase in carbonate–bearing bands, or lining pisolites in the granular varieties of Abu Marwat. Stilpnomelane is restricted to Wadi Kareim and Hadrabia, where it occurs as rare fine–grained fibrous crystals in chert bands (Essawy et al., 1997; Khalil and El-Shazly, 2012).

Table 1
Modal contents of selected BIF samples. All other mineral abbreviations are from Whitney and Evans (2010).

	Mag	Hem	Goe*	Qz	Chl/Oxychl	Ep	Grt	Cpx	Act	Ap	Plg	Cal*	Others
Um Nar													
N-6	X	X	tr	X		X			tr				
N-9	X	X		X	tr	X		M	M	tr			
N-53	X	M		X	tr	M				tr		M	Bt
N-23b	X	M	tr	X		M							
N12-58a	X	X		X			X	tr	X	tr			
N12-94	X	X				X	X			tr			Bt
N-10	X	X		X		X	M		M				
N-16	X	X		X		M	X						
N-18	X	X		X		M	X		M			M	
N-20	X	X		X	tr	M	M					M	
N-23a	X	X		X		M							
N12-26	M	X		X	tr	X	X						
N-28	X	X	tr	X		M	M					M	
N-58	X	X	tr	X		M				tr		M	
Carbonate rich													
N12-40		X		X	tr	X	X					X	
N12-29b	X	X		X	tr	M						X	
N12-31		X		X								X	
El Imra													
IM-8	X	X		X		M	X						
IM-27	X	X		X		X	X						
G. El Hadid													
H-3	X	M		X								M	
H-12	X	M		X							tr	X	
H-12a	X	X		X								X	
H-14a	X	M		X	tr						M	X	
H-21	X	M		X	tr							X	
H-26	X	M		X	tr						M	X	
H-37	X	M		X								M	
W. El Dabbah													
DB-100	X	X		X									
DB-102	X	X	tr	X									
DB-116	X		X	X									
DB-117	M	X		M									
DB-119	X	X	tr?	X		X				tr			sericite
DB-122	X	X		X						tr			
DB-127	X	X	X										
DB-141	X	X		M	X					tr	X		Rt
DB-147	X			X									
DB-156	X	X	tr	X									
DB-13–10	X	M		X		M	M						
DB-13-17b	tr	X	tr	X		X	X						
Carbonate facies													
DB-105	X	X		X	tr	X					X	X	sericite
Porous Ore													
DB-108	X	X		X									
Wadi Kareim: Magnetite facies													
K-*	X		X	M	tr						?		
K-4	M	X	tr	M								tr	
K-6	X	X	X	M	tr								
K-19	X	X	X	M									
Hematite facies													
K-11		X	X	M									
K-22		X	X	X						tr		X	
Carbonate rich													
K-5		tr	X	M	M							X	
K-7	tr	X	X	M	tr?							X	
porous ore													
K-8		X	X	X								M	
K-23	tr?	X	X	X								X	
K-24		X	X	X								X	
Abu marwat (granular)													
MW-11	X	X	X	X	X							X	
Gebel semna													
GS-12	X		X	X								M	
GS-16	X	X	X	X									

Mag: magnetite; Hem: hematite; Qz: quartz; Chl: chlorite; Oxychl: oxychlorite; Ep: Epidote; Grt: garnet; Cpx: diopside/ hedenbergite; Act: actinolite; Pl: plagioclase feldspar; Cal: calcite; X: major constituent; M: minor constinuent; tr: trace; * secondary.

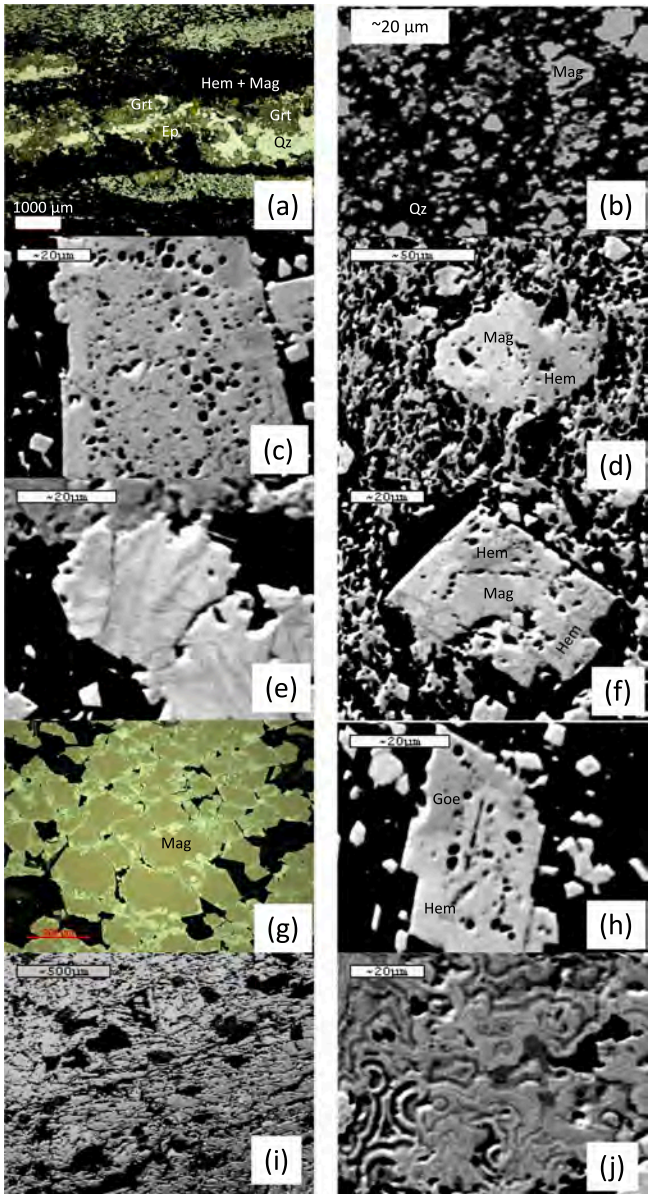

Fig. 4. Photomicrographs of (a) banded iron ore, N-20, Um Nar showing layers of magnetite III and hematite alternating with layers of garnet, epidote, quartz and dusty hematite; plane polarized transmitted light (PPL). (b) Backscattered electron image (BSEI) of magnetite I (bright) in quartz (black), with chlorite (grey), DB-119, Wadi El Dabbah. (c) BSEI of sieve textured magnetite II with inclusions of quartz, DB-141; Wadi El Dabbah. (d) BSEI of partially martitized magnetite II, DB-108; Wadi El Dabbah. (e) BSEI of magnetite II with oscillatory zoning, K-19; Wadi Kareim. (f) BSEI of magnetite II altered to hematite along its rim, DB-122; Wadi El Dabbah. (g) Magnetite III partially martitized along rim, N-53, Um Nar, polarized reflected light; (h) BSEI of magnetite II pseudomorphed by hematite and partially replaced by goethite (dark) along its rim, DB-141; Wadi El Dabbah. (i) BSEI of dense mass of specularite, N-58, Um Nar; (j) BSEI of colloform lepidocrocite, K-19, Wadi Kareim.

4.2. Host rocks

The banded iron formations in all 13 areas are intimately intercalated with very fine-grained metamorphosed mudstones or tuffs, which are in turn interbedded with metamorphosed lapilli tuffs and agglomerates and mafic metavolcanics (El-Shazly and Khalil, 2016). These rocks range from coarse-grained schists with the mineral assemblages: Hbl–Pl–Qz–Ep–Ilm–Ttn–Ap and Grt–Bt–Ms–Qz in the southern outcrops (Um Nar & El Imra), to fine-grained metabasalts, metadolerites and metatuffs with relict igneous minerals and textures and the assemblages: Act–Ab–Ep–Qz–Chl–Ttn–Ap and Ms–Chl–Qz–Ttn in the northern outcrops (e.g. Wadi Kareim and Abu Marwat). Detailed textural and mineral chemical data for these rocks were presented in El-Shazly and Khalil (2014, 2016).

5. Geochemistry

5.1. Banded iron formations

5.1.1. Major and trace elements

The eight BIF deposits studied in this work have a higher average concentration of Fe (*c.* 44 wt%) compared to the average Fe concentrations reported for Algoma or Superior type deposits (*c.* 28 wt%, e.g. Gross and McLeod, 1980). These CED BIFs have highly variable SiO_2 and Fe_2O_{3T} values that range from 14 to 60% and 32 to 86% by weight, respectively (Table 2). This variation occurs within each deposit, where the highest Fe_2O_3 (and lowest SiO_2) values characterize the most strongly weathered samples (e.g. the ochres of Gebel Semna GS-3, 4, 5, and 16; Table 2). On the other hand, the highest silica values are recorded for the porous samples K-8, K-22, and K-24 of Wadi Kareim, or those with a substantial amount of lithic fragments (e.g. DB-119 and 141 of Wadi El-Dabbah; Tables 1 and 2). Figure 5 shows this large variation in Si and Fe^T values, and the lack of any clustering of data points related to specific areas. Moreover, no clear correlation exists between Fe content and alteration/ weathering Fig. 5, as demonstrated by Fig. 5 and the lack of any correlation between Fe^T and LOI or indices of weathering or chemical alteration.

Most CED BIF deposits are characterized by a relatively low Al_2O_3 content (0.1 to 1.2 wt%) compared to average Superior or Algoma type deposits (1.5–3.7 wt%; e.g. Gross and McLeod, 1980), although BIFs from El Imra and Wadi El Dabbah (and a few outliers from other deposits) show significantly higher values (*c.* 4 wt% or higher; Fig. 6). For most silicate/ oxide facies BIF samples, CaO ranges from 0.3 to 8 wt%, with the highest values recorded for samples from El Imra. On the other hand, a few carbonate–rich samples from Um Ghamis and Wadi Kareim have CaO values in the range 10–13.5 wt%. MgO is a minor constituent of all BIFs with values < 1%, although samples from El Imra, Gebel El Hadid, Um Ghamis, and Wadi El Dabbah are characterized by higher concentrations of ~2.5 wt%. TiO_2 is another minor constituent (< 0.5 wt%) of all deposits, except for those few samples with clusters of ilmenite (Wadi El Dabbah, Um Ghamis). P_2O_5 ranges from 0.21 to 2.83 wt% (average 0.96 ± 0.81), with the highest values recorded for Wadi El Dabbah (average 2.13 ± 0.99), and the lowest for Um Nar (average 0.46 ± 0.16; Table 2).

With the exception of the very strongly altered ochres from Gebel Semna, trace element concentrations in the BIFs are rather low and highly variable. Average concentrations in ppm for Sc, V, Cr, Co, Ni, Cu, and Zn are 6 ± 3.2, 54 ± 22, 215 ± 19; 58 ± 64, 14 ± 18, 17 ± 28, and 23 ± 24, respectively (Table 2). Ba values range from 20 to 65 ppm with a few samples recording values as high as 250 ppm; whereas Sr concentrations range from 38 to 210 ppm with some carbonate - rich samples recording values as high as 632 ppm (K-22; Table 2). Concentrations of the high field strength elements Y, Zr, and Nb, are generally low and highly variable for most areas (Table 2). Fig. 6 shows these geochemical trends across the CED, which reveal that BIF samples from El Imra are characterized by the highest FeO, MnO, CaO, V, Sc, and Ni, whereas Wadi El Dabbah BIFs record the highest values for Al_2O_3, TiO_2, P_2O_5, Y, Zr, La, and Ce.

5.1.2. Fe^{2+}/Fe^{3+} ratios

Fe^{2+}/Fe^{3+} ratios for all CED BIFs range from 0.01 to 0.84, with samples from El Imra and porous samples from Wadi Kareim recording the highest and lowest values, respectively (Table 2). A plot of Fe^{2+}/Fe^{3+} against Fe_T/Si or total Fe (Fe_T) shows no correlation with either parameter (Fig. 7). Nevertheless, visibly weathered samples with

Table 2
Whole rock chemical compositions of BIFs.

	Um Nar										El Imra				Gebel Hadid				
	N-9	N-10	N-16	N-25	N-18	N-20	**N-23**	N-28	N-53	N-58	IM-22	IM-27	H-3	H-12	H12a	**H-14a**	H-21	H-26	H-37
Lab	Acme	Acme	Acme	Acme	ALS-61	ALS-81	ALS-81	ALS-61	ALS-61	ALS-81	ALS-81	ALS-81	Acme	Acme	Acme	Acme	Acme	Acme	Acme
SiO_2	61.61	29.23	40.33	16.28	22.37	15.30	49.77	23.89	27.49	19.00	32.03	12.73	9.85	21.77	54.86	31.84	46.94	42.03	15.42
TiO_2	0.03	0.17	0.05	0.03	0.11	0.09	0.08	0.09	0.11	0.09	0.03	0.06	0.03	0.06	0.03	0.42	0.07	0.27	0.10
Al_2O_3	0.48	3.22	0.45	0.13	1.22	0.95	0.59	0.51	1.84	0.45	3.52	4.60	0.17	0.69	0.40	9.93	2.46	6.28	1.91
Fe_2O_3T	35.88	60.15	53.11	81.38	67.85	82.02	44.20	69.59	67.17	77.07	58.73	76.33	87.80	74.16	41.92	33.55	41.40	44.30	74.54
Fe_2O_3	27.23	54.80	49.91	75.81	66.04	74.66	39.04	65.51	50.18	72.46	32.04	47.68	84.16	72.02	39.11	29.62	38.85	42.12	71.41
FeO	7.86	4.86	2.91	5.06	1.65	6.69	4.69	3.71	15.45	4.19	24.26	26.05	3.21	1.92	2.49	3.48	2.28	1.95	2.81
MnO	0.09	0.16	0.05	< 0.01	0.43	0.09	0.08	0.08	0.09	0.05	0.24	0.16	0.06	0.02	0.04	0.21	0.10	0.10	0.10
MgO	0.10	0.83	0.02	< 0.01	0.23	0.05	0.13	0.11	0.12	0.08	1.92	0.30	0.05	0.13	0.02	2.73	0.76	2.41	2.05
CaO	1.78	4.33	3.46	1.08	5.96	1.65	1.65	1.70	2.39	1.46	3.98	6.76	1.07	1.74	1.50	8.26	3.67	1.15	2.30
Na_2O	< 0.01	< 0.01	< 0.01	< 0.01	0.01	0.03	0.06	0.17	0.10	0.04	0.14	0.06	0.02	0.10	0.10	4.04	0.05	0.78	< 0.01
K_2O	0.09	0.02	< 0.01	0.01	0.28	0.32	0.41	0.29	0.16	0.29	0.21	0.17	< 0.01	0.02	< 0.01	0.13	0.06	1.15	< 0.01
P_2O_5	0.40	0.39	0.31	0.57	0.27	0.60	0.37	0.62	0.75	0.29	0.77	0.77	0.57	0.75	0.45	0.32	0.43	0.52	0.44
LOI	0.50	1.40	0.20	0.50	0.86	0.00	0.15	0.32	0.00	1.37	0.00	0.00	0.30	0.50	0.70	8.50	4.00	0.90	3.00
Total	100.17	99.41	97.69	99.47	99.43	100.42	97.01	96.99	98.68	99.77	99.15	99.32	99.44	99.72	99.70	99.48	99.67	99.66	99.54
Sc	5.0	7.0	3.0	4.0	4.0	4.0	2.0	3.0	4.0	5.0	10.0	12.0	4.0	5.0	3.0	11.0	9.0	11.0	6.0
V	72.0	78.0	64.0	59.0	35.0	46.0	35.0	59.0	53.0	51.0	115.0	94.0	64.0	57.0	32.0	52.0	82.0	91.0	56.0
Cr	54.6	20.5	40.9	13.6	< 10	< 10	< 10	< 10	< 10	< 10	30.0	30.0	78.4	51.2	64.8	34.1	23.9	40.9	47.7
Co	1.6	3.0	0.7	< 0.2	58.0	58.0	216.0	160.0	85.0	64.0	15.0	52.0	1.5	0.7	0.5	6.4	2.1	2.4	1.6
Ni	46.0	< 20	42.0	< 20	< 20	< 20	< 20	< 20	< 20	< 20	44.0	55.0	67.9	32.8	64.8	24.5	22.5	36.1	41.1
Cu	1.4	1.0	0.6	0.2	0.7	3.0	0.9	0.6	0.8	0.9	19.0	17.5	15.2	1.7	2.8	8.4	15.5	15.7	3.9
Zn	9.0	16.0	3.0	1.0	7.0	5.0	8.0	5.0	7.0	2.0	22.0	1.0	5.0	8.0	6.0	37.0	28.0	60.0	11.0
Ba	25.0	9.0	6.0	2.0	10.0	4.6	20.6	10.0	8.0	8.2	30.7	100.5	40.0	7.0	2.0	84.0	37.0	249.0	6.0
Sr	38.6	151.3	38.6	40.5	518.0	175.0	115.0	54.0	45.0	63.0	30.9	50.9	37.9	81.4	107.0	220.4	48.5	37.9	61.0
Y	15.7	22.1	15.7	17.8	29.0	27.1	19.7	20.2	31.0	24.7	20.9	30.9	18.6	30.3	18.2	38.3	21.9	23.8	23.2
Zr	19.4	42.4	9.0	6.9	4.3	6.0	2.0	8.2	5.5	10.0	47.0	59.0	6.9	14.5	7.3	97.3	41.8	89.3	20.6
Nb	0.4	1.7	0.3	0.2	29.0	4.7	23.2	33.0	39.0	5.9	2.1	7.9	0.2	0.4	0.3	3.3	1.9	2.4	0.7
La	3.4	3.0	1.4	1.4	2.7	2.8	5.1	2.6	6.6	4.9	9.2	24.6	1.2	4.0	2.3	9.8	8.8	8.0	4.9
Ce	8.2	6.6	3.7	3.7	38.5	6.4	10.9	19.6	27.0	29.5	21.3	47.4	2.5	9.9	4.5	24.9	25.1	20.2	10.5
Pr	1.1	1.0	0.5	0.6	n.d.	1.0	1.5	n.d.	1.0	1.8	3.1	6.0	0.4	1.7	0.8	3.4	3.5	2.6	1.5
Nd	5.3	4.8	2.8	3.4	n.d.	5.4	7.3	n.d.	5.7	8.9	14.6	26.8	2.2	8.0	3.5	15.9	16.2	11.4	6.7
Sm	1.2	1.1	0.6	0.8	n.d.	1.4	1.5	n.d.	1.4	2.0	3.8	6.0	0.6	1.7	0.8	3.5	3.5	2.7	1.4
Eu	0.3	0.3	0.2	0.2	n.d.	0.3	0.4	n.d.	0.4	0.5	0.7	1.4	0.2	0.7	0.3	0.9	0.8	0.7	0.4
Gd	1.7	1.5	1.0	1.2	n.d.	1.6	2.0	n.d.	2.1	2.5	4.3	6.0	1.0	2.4	1.3	4.1	4.1	3.0	2.0
Tb	0.3	0.3	0.2	0.2	n.d.	0.3	0.3	n.d.	0.3	0.4	0.7	1.0	0.2	0.5	0.2	0.8	0.7	0.5	0.4
Dy	1.9	2.2	1.5	1.7	n.d.	2.4	2.3	n.d.	2.5	2.9	4.9	6.8	1.5	3.3	1.8	5.0	4.0	3.5	2.7
Ho	0.4	0.6	0.4	0.4	n.d.	0.7	0.5	n.d.	0.6	0.7	1.1	1.7	0.4	0.9	0.5	1.2	0.9	0.8	0.7
Er	1.4	2.1	1.5	1.4	n.d.	2.2	1.6	n.d.	1.9	2.3	3.3	5.0	1.5	2.8	1.6	3.7	2.5	2.6	2.2
Tm	0.2	0.3	0.2	0.2	n.d.	0.3	0.3	n.d.	0.3	0.4	0.5	0.7	0.2	0.4	0.3	0.6	0.4	0.4	0.3
Yb	1.5	2.4	1.6	1.1	n.d.	2.3	1.4	n.d.	1.9	2.4	3.3	4.5	1.7	2.9	1.6	4.0	2.5	2.9	2.3
Lu	0.2	0.4	0.3	0.2	n.d.	0.4	0.2	n.d.	0.4	0.4	0.5	0.7	0.3	0.5	0.3	0.7	0.4	0.5	0.4
ΣREE	27.11	26.43	15.72	16.52	n.d.	27.35	35.26	n.d.	52.19	59.54	71.42	138.61	13.86	39.37	19.56	78.31	73.26	59.72	36.31
Y/Ho	36.51	38.10	40.26	44.50	n.d.	41.69	37.17	n.d.	50.00	34.79	18.50	18.73	44.29	35.65	37.92	31.65	25.47	29.38	35.15
Sm/Lu	5.22	2.84	2.14	4.17	n.d.	3.91	7.00	n.d.	3.63	5.13	7.17	8.51	2.18	3.62	3.08	5.07	9.08	5.76	3.84
Pr/Yb	0.75	0.42	0.33	0.56	n.d.	0.43	1.04	n.d.	0.54	0.76	0.92	1.33	0.25	0.58	0.47	0.85	1.44	0.90	0.64

(*continued on next page*)

Table 2 (*continued*)

	Um Ghamis					Wadi El Dabbah								Wadi Kareim			
	GH-3	GH-25	GH-22	GH-31	GH-32	**DB-108**	DB-141	DB-115	DB-146	DB-155	D12-10	**D13-17b**	K-1	**K-4**	**K-6**	***K-7***	***K-8***
Lab	Acme	MU	MU	Acme	Acme	ALS-61	ALS-81	ALS-61	ALS-61	ALS-61	ALS-81	ALS-81	MU	ALS-61	ALS-81	ALS-61	ALS-81
SiO_2	20.87	29.16	22.41	25.41	24.02	25.34	41.29	38.91	35.97	18.43	41.21	30.44	37.88	43.07	16.35	16.44	60.79
TiO_2	1.58	3.81	0.23	3	0.19	0.15	0.47	0.17	0.35	0.16	0.11	0.22	0.27	0.07	0.15	0.10	0.04
Al_2O_3	0.09	0.18	2.81	0.17	2.71	3.29	7.32	3.05	8.11	1.54	2.66	5.71	1.11	0.81	0.92	0.90	0.59
Fe_2O_3T	52.89	57.66	71.10	64.91	65.53	65.65	45.20	51.01	43.25	76.40	41.57	53.64	56.56	51.67	78.25	65.73	31.93
Fe_2O_3	49.172	49.96	59.96	64.272	56.59	61.97	33.76	47.87	39.62	73.31	39.60	48.88	48.59	45.62	70.50	63.92	30.74
FeO	3.38	7	10.13	0.58	8.06	3.35	10.40	2.86	3.30	2.81	1.79	4.33	7.25	5.50	7.04	1.65	1.08
MnO	0.17	0.05	0.07	0.11	0.06	0.08	0.12	0.06	0.10	0.08	0.02	0.09	0.15	0.06	0.09	0.24	0.05
MgO	0.55	0.51	0.84	0.86	0.74	1.16	2.19	1.04	2.47	0.61	0.08	1.52	0.22	0.08	0.28	0.36	0.13
CaO	13.44	3.6	2.06	2.31	2.30	0.41	0.34	2.11	4.59	2.14	7.11	9.13	0.32	1.53	0.96	7.80	0.99
Na_2O	0.07	1.45	1.01	0.27	1.09	0.31	2.46	0.38	1.38	0.39	0.67	0.07	0.07	0.07	0.02	0.04	0.19
K_2O	0.04	0.3	0.15	0.48	0.37	0.10	0.09	0.16	0.15	0.26	0.27	0.10	0.09	0.15	0.31	0.06	0.62
P_2O_5	1.93	2.21	1.26	1.43	1.43	1.70	1.80	1.45	1.83	1.50	4.34	1.87	0.23	0.30	1.44	2.29	0.26
LOI	8.30	0.90	0.79	0.90	1.05	1.92	1.11	1.34	2.62	0.00	1.73	0.71	6.19	1.55	2.14	7.20	2.99
Total	99.59	99.13	101.71	99.79	98.60	99.78	101.34	99.39	100.48	101.23	99.58	103.05	102.35	98.81	100.21	100.99	98.47
Sc	5.0	7.0	7.9	10.0	11.0	5.0	10.0	5.0	9.0	7.0	7.0	9.8	12.6	3.0	7.0	5.0	3.0
V	29.0	65.0	68.7	87.0	63.0	49.0	69.0	64.0	76.0	77.0	60.0	86.0	49.8	44.0	66.0	31.0	70.0
Cr	20.0	20.0	12.0	40.0	61.2	< 10	< 10	< 10	11.0	< 10	< 10	25.0	< 10	< 10	10.0	< 10	< 10
Co	35.4	71.1	94.0	60.7	43.1	11.0	88.0	63.0	92.0	34.0	18.0	13.0	1.2	280.0	202.0	34.0	148.0
Ni	< 20	< 20	< 20	< 20	< 20	< 20	< 20	< 20	< 20	< 20	< 20	43.0	< 20	< 20	< 20	< 20	< 20
Cu	18.1	16.6	24.1	72.6	3.9	4.0	4.0	8.0	7.0	3.0	18.0	20.0	106.0	14.0	4.0	34.0	162.0
Zn	25.0	21.0	87.0	50.0	22.0	13.0	58.0	25.0	33.0	11.0	0.0	23.5	< 1	2.0	4.0	8.0	10.0
Ba	18.0	83.0	102.0	138.0	101.0	20.0	20.0	30.0	40.0	20.0	51.5	26.1	55.1	10.0	20.0	40.0	20.0
Sr	169.7	117.0	69.0	34.8	95.0	40.0	63.0	53.0	102.0	48.0	97.6	208.0	188.0	35.0	133.0	951.0	104.0
Y	39.5	38.8	27.0	30.6	25.6	41.6	38.2	45.4	61.4	54.8	27.5	29.0	8.0	7.1	10.0	22.4	15.0
Zr	17.5	40.2	33.0	43.3	27.8	35.5	198.0	4.1	6.5	25.7	27.0	60.0	7.5	23.6	10.0	14.3	15.0
Nb	0.3	2.3	1.9	3.6	2.3	1.9	7.1	1.5	1.6	1.8	1.7	3.1	3.5	1.8	7.7	1.3	14.4
La	5.8	9.9	5.5	9.7	5.7	5.2	4.6	10.0	24.4	14.9	4.8	7.9	7.4	1.8	19.4	49.7	2.3
Ce	13.6	18.7	11.8	24.4	11.9	53.4	12.5	38.0	56.1	55.9	11.5	15.9	10.4	26.8	42.9	73.4	5.6
Pr	2.1	2.9	1.7	3.3	1.7	n.d.	1.9	n.d.	n.d.	n.d.	1.8	2.4	2.6	n.d.	6.0	n.d.	0.8
Nd	10.3	13.1	8.5	16.2	8.3	n.d.	9.3	n.d.	n.d.	n.d.	9.0	11.3	12.4	n.d.	31.0	n.d.	3.9
Sm	2.1	3.3	1.9	3.4	1.8	n.d.	2.3	n.d.	n.d.	n.d.	2.0	2.8	2.7	n.d.	7.0	n.d.	0.7
Eu	0.7	0.8	0.5	0.7	0.6	n.d.	0.7	n.d.	n.d.	n.d.	0.6	0.7	0.5	n.d.	1.5	n.d.	0.2
Gd	3.0	4.3	2.7	4.6	2.6	n.d.	3.5	n.d.	n.d.	n.d.	2.6	3.4	2.9	n.d.	8.7	n.d.	1.1
Tb	0.5	0.8	0.5	0.8	0.4	n.d.	0.5	n.d.	n.d.	n.d.	0.4	0.6	0.7	n.d.	1.5	n.d.	0.1
Dy	3.9	5.4	3.4	5.0	3.3	n.d.	3.6	n.d.	n.d.	n.d.	3.3	4.1	3.4	n.d.	10.1	n.d.	1.0
Ho	1.0	1.2	0.8	1.1	0.8	n.d.	0.7	n.d.	n.d.	n.d.	0.8	1.0	1.1	n.d.	2.6	n.d.	0.1
Er	3.3	3.7	2.5	3.5	2.4	n.d.	2.2	n.d.	n.d.	n.d.	2.5	2.9	3.8	n.d.	7.5	n.d.	0.7
Tm	0.5	0.5	0.4	0.5	0.3	n.d.	0.3	n.d.	n.d.	n.d.	0.4	0.4	0.5	n.d.	1.1	n.d.	0.1
Yb	3.1	3.5	2.6	3.3	2.3	n.d.	2.1	n.d.	n.d.	n.d.	2.7	2.9	2.2	n.d.	6.1	n.d.	0.8
Lu	0.5	0.5	0.4	0.6	0.4	n.d.	0.3	n.d.	n.d.	n.d.	0.4	0.5	0.4	n.d.	1.0	n.d.	0.1
ΣREE	50.18	68.56	43.01	77.08	42.47	n.d.	44.57	n.d.	n.d.	n.d.	42.71	56.82	50.96	n.d.	146.40	n.d.	17.50
Y/Ho	39.50	31.54	33.75	26.84	32.41	n.d.	51.62	n.d.	n.d.	n.d.	34.81	28.71	7.48	n.d.	3.83	n.d.	107.14
Sm/Lu	4.16	6.54	4.92	6.24	5.11	n.d.	6.76	n.d.	n.d.	n.d.	4.83	6.27	7.30	n.d.	6.80	n.d.	5.54
Pr/Yb	0.67	0.85	0.65	1.01	0.73	n.d.	0.88	n.d.	n.d.	n.d.	0.67	0.83	1.17	n.d.	0.98	n.d.	1.00

(*continued on next page*)

Table 2 (*continued*)

	Gebel Semna													Abu Marwat		
	K-11	K-16	**K19**	***K-22***	***K-24***	***GS-5***	***GS-4***	***GS-3***	***GS-16***	GS17-1	GS17-2	GS17-3	GS17-4	MW-10	**MW-21**	**MW-11**	**MW-16**
Lab	ALS-81	MU	ALS-81	ALS-61	ALS-81	MU	ALS-81	ALS-81	ALS-81	MU	MU	MU	MU	ALS-81	ALS-81	Acme	Acme
SiO_2	18.46	42.91	23.45	41.53	29.78	11.74	31.08	8.28	29.40	40.21	49.49	29.62	55.20	24.17	18.66	17.08	22.85
TiO_2	0.08	0.08	0.12	0.07	0.10	0.15	0.20	0.01	0.01	0.43	0.15	0.47	0.12	0.06	0.07	0.08	0.08
Al_2O_3	1.01	0.39	0.70	0.38	0.87	0.49	1.29	0.63	2.55	7.90	0.84	6.73	1.80	0.97	1.04	0.89	0.29
Fe_2O_3T	71.16	52.22	72.99	33.58	41.92	64.15	52.87	68.28	45.07	42.06	43.49	53.11	41.29	67.36	72.43	66.76	70.16
Fe_2O_3	70.03	37.93	64.11	33.16	41.08	63.45	52.24	67.72	44.87	23.77	34.95	35.39	34.56	59.24	73.06	63.30	65.60
FeO	1.03	12.99	8.07	0.38	0.76	0.64	0.57	0.51	0.19	16.62	7.76	16.11	6.12	7.38	2.15	3.15	4.15
MnO	0.05	0.06	0.05	0.10	0.19	0.14	0.09	0.45	0.38	0.14	0.07	0.10	0.11	0.08	0.08	0.09	< 0.01
MgO	0.12	0.10	0.52	0.27	0.36	0.21	0.21	2.02	11.37	2.72	0.37	2.52	0.81	0.67	0.54	1.17	0.02
CaO	0.90	2.06	0.84	10.98	11.40	9.41	1.35	0.84	1.98	1.94	5.04	3.12	1.61	2.97	3.56	7.38	1.01
Na_2O	0.02	0.24	0.01	0.04	0.04	0.54	0.87	3.14	0.76	1.54	0.00	1.52	0.23	0.06	0.05	< 0.01	< 0.01
K_2O	0.10	0.00	0.55	0.31	0.35	0.22	0.29	0.48	0.06	0.02	0.02	0.00	0.00	0.13	0.11	< 0.01	< 0.01
P_2O_5	1.33	0.15	0.46	2.22	0.46	0.26	0.26	0.08	0.14	1.07	2.19	0.84	0.55	0.74	0.98	1.11	0.53
LOI	6.20	1.40	1.23	8.07	14.52	12.01	7.07	14.64	7.05	3.19	0.89	3.41	1.26	2.49	2.49	5.30	4.80
Total	99.32	98.31	100.1	97.51	99.89	99.27	95.53	98.80	98.75	99.55	101.78	99.83	102.36	98.96	102.79	99.55	99.33
Sc	5.0	6.4	5.0	3.0	4.0	6.0	3.0	1.0	16.0	15.4	5.8	12.3	6.7	6.0	< 1	3.0	4.0
V	59.0	14.2	59.0	20.0	36.0	111.0	107.0	27.0	161.0	14.7	16.9	22.9	16.1	63.0	58.0	33.0	38.0
Cr	10.0	< 10	< 10	< 10	< 10	100.0	100.0	15.0	90.0	14.9	22.6	32.7	35.2	20.0	10.0	20.0	30.0
Co	109.0	2.5	18.3	55.0	32.0	52.3	30.2	7.0	11.0	134.0	135.0	166.0	131.0	7.0	11.0	70.4	108.5
Ni	< 20	< 20	< 20	< 20	< 20	< 20	< 20	35.0	205.0	< 20	< 20	< 20	< 20	< 20	7.6	< 20	< 20
Cu	10.0	5.0	0.5	6.0	20.0	1710	2030	4510	7350	8.6	11.3	62.1	12.5	43.0	18.5	2.8	3.5
Zn	14.0	8.0	6.0	4.0	12.0	23.2	597	4510	1525	95.8	36.8	51.5	50.4	30.0	39.7	11.0	6.0
Ba	30.0	1.6	20.0	20.0	90.0	90.2	790.0	530.0	600.0	40.2	48.9	17.0	55.0	40.0	21.0	58.0	8.0
Sr	117.0	65.7	111.0	632.0	153.0	145.0	98.0	59.0	119.0	207.0	104.2	276.3	53.8	50.5	70.0	81.0	28.8
Y	20.4	8.5	25.5	77.2	26.6	n.d.	4.9	0.9	4.1	36.1	72.4	43.0	27.3	26.8	31.5	19.4	19.5
Zr	5.0	< 2	94.0	110.0	39.0	n.d.	35.0	11.0	8.0	81.0	10.9	82.4	16.3	30.0	15.0	10.1	9.9
Nb	4.5	4.1	3.0	1.0	2.5	4.6	3.2	0.3	< 0.2	< 0.2	3.8	< 0.2	< 0.2	3.3	1.2	2.2	2.8
La	5.2	3.0	7.8	12.6	5.3	4.2	< 0.5	< 0.5	< 0.5	5.8	20.1	12.0	6.3	5.6	6.9	3.8	1.9
Ce	11.3	31.6	19.1	67.7	12.2	6.8	0.5	< 0.5	< 0.5	6.2	24.9	20.6	6.5	27.0	14.7	9.3	4.3
Pr	1.7	n.d.	2.6	n.d.	1.7	n.d.	0.1	0.0	< 0.03	n.d.	n.d.	n.d.	n.d.	1.7	2.1	1.3	0.6
Nd	8.0	n.d.	12.4	n.d.	8.6	n.d.	0.5	0.2	0.3	n.d.	n.d.	n.d.	n.d.	8.1	9.5	6.1	3.2
Sm	1.6	n.d.	2.7	n.d.	2.0	n.d.	0.2	0.1	0.6	n.d.	n.d.	n.d.	n.d.	1.9	1.8	1.2	1.0
Eu	0.4	n.d.	0.7	n.d.	0.6	n.d.	0.1	0.1	0.3	n.d.	n.d.	n.d.	n.d.	0.5	0.5	0.3	0.3
Gd	2.7	n.d.	3.1	n.d.	3.1	n.d.	0.7	< 0.05	1.0	n.d.	n.d.	n.d.	n.d.	2.6	2.4	1.7	1.7
Tb	0.4	n.d.	0.5	n.d.	0.3	n.d.	0.1	< 0.01	0.1	n.d.	n.d.	n.d.	n.d.	0.5	0.5	0.3	0.3
Dy	3.6	n.d.	3.9	n.d.	3.2	n.d.	0.8	0.2	1.0	n.d.	n.d.	n.d.	n.d.	3.7	3.6	2.1	2.3
Ho	1.7	n.d.	0.7	n.d.	0.8	n.d.	0.1	< 0.01	0.1	n.d.	n.d.	n.d.	n.d.	0.9	1.0	0.5	0.6
Er	4.2	n.d.	2.7	n.d.	2.1	n.d.	0.6	0.1	0.5	n.d.	n.d.	n.d.	n.d.	2.7	3.0	1.8	1.8
Tm	0.4	n.d.	0.4	n.d.	0.4	n.d.	0.1	0.0	0.1	n.d.	n.d.	n.d.	n.d.	0.4	0.5	0.3	0.3
Yb	2.9	n.d.	3.0	n.d.	2.1	n.d.	0.7	0.1	0.4	n.d.	n.d.	n.d.	n.d.	2.6	2.9	1.6	1.6
Lu	0.5	n.d.	0.5	n.d.	0.4	n.d.	0.1	0.0	0.1	n.d.	n.d.	n.d.	n.d.	0.4	0.5	0.3	0.3
ΣREE	44.48	n.d.	60.05	n.d.	42.69	n.d.	4.52	0.77	4.48	n.d.	n.d.	n.d.	n.d.	58.56	49.75	30.56	20.22
Y/Ho	12.00	n.d.	34.46	n.d.	32.84	n.d.	44.55	n.d.	37.27	n.d.	n.d.	n.d.	n.d.	29.13	32.47	38.04	30.95
Sm/Lu	3.62	n.d.	5.74	n.d.	4.64	n.d.	1.55	4.00	8.00	n.d.	n.d.	n.d.	n.d.	4.35	3.81	4.56	3.64
Pr/Yb	0.60	n.d.	0.86	n.d.	0.83	n.d.	0.64	n.d.	n.d.	n.d.	n.d.	n.d.	n.d.	0.64	0.71	0.77	0.39

Major element results in weight%, trace element concentrations in ppm. Samples in bold are hydrothermally altered, those in italics are weathered. Acme and ALS-81: analyses performed in Acme Labs, Canada, and ALS minerals, Reno, NV, respectively.

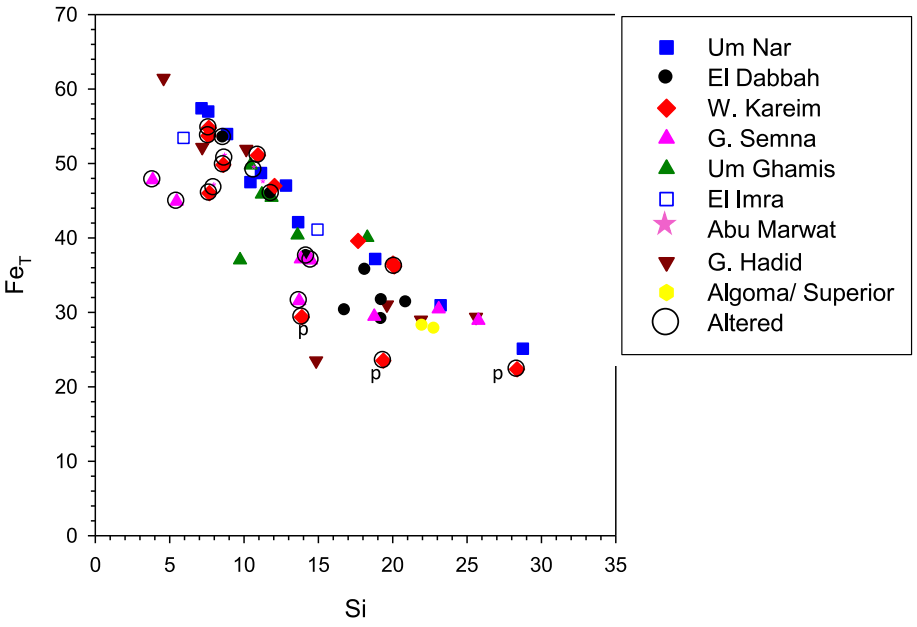

Fig. 5. Total iron (Fe^T) vs. Si plot for all deposits compared with the average values for Algoma and Superior type BIFs. "Altered" represents samples affected by hydrothermal alteration and/ or weathering (defined as those with significant amounts of secondary calcite/ goethite/ lepidocrocite), "p" represents those samples with a "porous" texture.

significant amounts of lepidocrocite and/ or goethite are characterized by the lowest Fe^{2+}/Fe^{3+} ratios (< 0.15), despite having a wide range of Fe_T values (Fig. 7).

5.1.3. Rare earth elements

Although REE are a subset of trace elements discussed above, they merit a more detailed discussion given that their concentrations are unaffected by diagenesis, making them instrumental in understanding the origin of BIFs (e.g. Graf, 1978; Fryer, 1977, 1983; Derry and Jacobsen, 1990; Kato et al., 2006; Thurston et al., 2012; Cox et al., 2013). The importance of REE also stems from their fractionation between various phases in equilibrium as a result of differences in ionic radii, and in a few cases, their oxidation states. In this study, we have chosen to normalize BIF concentrations to the Post Archean Australian Shale (PAAS; e.g. Nance and Taylor, 1976), and to include Y on the REE diagrams, since Y is a REE whose ionic size falls between that of Dy and Ho. These REY diagrams therefore allow for the evaluation of the "Y anomaly" (Bau and Dulski, 1996, 1999; Zhang and Nozaki, 1996), and its significance in tracing the effects of hydrothermal fluids on BIF genesis (e.g. Cox et al., 2013).

All BIF samples analyzed in this study are characterized by PAAS normalized LREE depleted patterns and values between 0.03 and 1 (except for Gebel Semna ochres which have much lower total REE contents; Fig. 8), whereas a few samples from Um Nar, Gebel El Hadid, Um Ghamis, and Wadi Kareim, show a weak negative Ce anomaly (Fig. 8). A few samples from Um Nar, Gebel El Hadid, Um Ghamis, and Wadi El Dabbah have a weak positive Eu anomaly (1.02–1.2). Similarly, a few samples from Um Nar, Gebel El Hadid, Gebel Semna, and Abu Marwat show a positive Y anomaly, whereas most samples from El Imra and Wadi Kareim show a distinct negative Y signature. Average Y/Ho values for each deposit range mostly from 30 to 50, with the exception of El Imra characterized by a low value of 18.6 ± 0.16, and a few notable outliers of strongly altered/ weathered samples from Wadi Kareim and Gebel Semna (Table 2). Average Pr/Yb values range from 0.6 for Um Nar to 1.12 for El Imra, whereas average Sm/Lu values range from 4.08 ± 0.4 for Abu Marwat to 7.8 ± 0.9 for El Imra.

5.2. Host rocks

5.2.1. Metavolcanic rocks

With the exception of IM-1 from El Imra, all metavolcanic rocks range in composition from basalts to rhyolites (SiO_2 = 46–77 wt%, Table 3; Fig. 9a). All samples except N12-7 are characterized by a tholeiitic to calc-alkalic character as revealed by plots of SiO_2 vs. K_2O (Peccerillo and Taylor, 1976) and Nb/Y vs. Zr/P_2O_5 (Floyd and Winchester, 1978), and a Y/Nb > 1 (Supplementary Fig. 1; Table 3). Almost all samples show a clear subduction–related signature indicated by TiO_2 < 1.5, Ba/La > 15, and relatively high La/Nb ratios (Table 3). Such a signature is also confirmed by a Nb trough on the N-MORB normalized spider diagrams of Sun and McDonough (1989) (Supplementary Fig. 1c).

On the tectonic discrimination diagrams of Pearce and Cann (1973), Pearce and Norry (1979), Pearce (1982), or Meschede (1986), the samples scatter over the fields of mid-oceanic ridge (MORB), island arc (IAT), volcanic arc (VAB), within plate (WPB), and calc-alkali (CAB) basalts, with some clustering of data points in the fields of IAT/ CAB that is particularly obvious for samples from Wadi El Dabbah. Plotting all samples on the Th/Yb vs. Nb/Yb diagram of Pearce (2014) reveals an arc-related origin for all metavolcanics except N12-27, with samples from Um Nar falling closest to the field of MORB (Fig. 9b). This arc-related signature is further confirmed by a positive correlation (single trend; R^2 = 0.76) between Ce and Yb (Hawkesworth et al., 1993a). Based on their Ti/V ratios, most of these arc-related rocks from Um Nar, El Imra, Um Ghamis, Wadi Kareim, and Abu Marwat plot in the "slab-distal" back- or fore-arc basin field, whereas almost all samples from Wadi El Dabbah fall in the IAT/ "slab-proximal" back- or fore-arc basin basalt field of Shervais (1982) (Fig. 9c). The discriminant diagram of Hollocher et al., (2012) shows most samples straddling the fields of oceanic arcs and continental arcs, with Um Nar samples falling closest to the MORB field (Fig. 9d).

Applying the discriminant functions of Agrawal et al. (2008) to the basic metavolcanics shows that the Um Nar samples are mostly MORBs, whereas most other samples are island arc basalts (Fig. 9e–h). Although it is nearly impossible to differentiate MORB from back-arc or fore-arc basin basalts geochemically (e.g. Pearce, 2014; Li et al., 2015), it is worth mentioning that on the Y/15–La/10–Nb/8 diagram of Cabanis and Lecolle (1989), most rocks from Um Nar, El Imra, and Um Ghamis plot in the volcanic arc basalt fields, whereas most of the Wadi El Dabbah samples fall in the back arc basin field, and most samples from Abu Marwat fall in the MORB field. On the other hand, samples from Wadi Kareim fall in the volcanic arc and back arc basin fields (Fig. 9j). Most metavolcanic rocks are characterized by flat to slightly LREE -

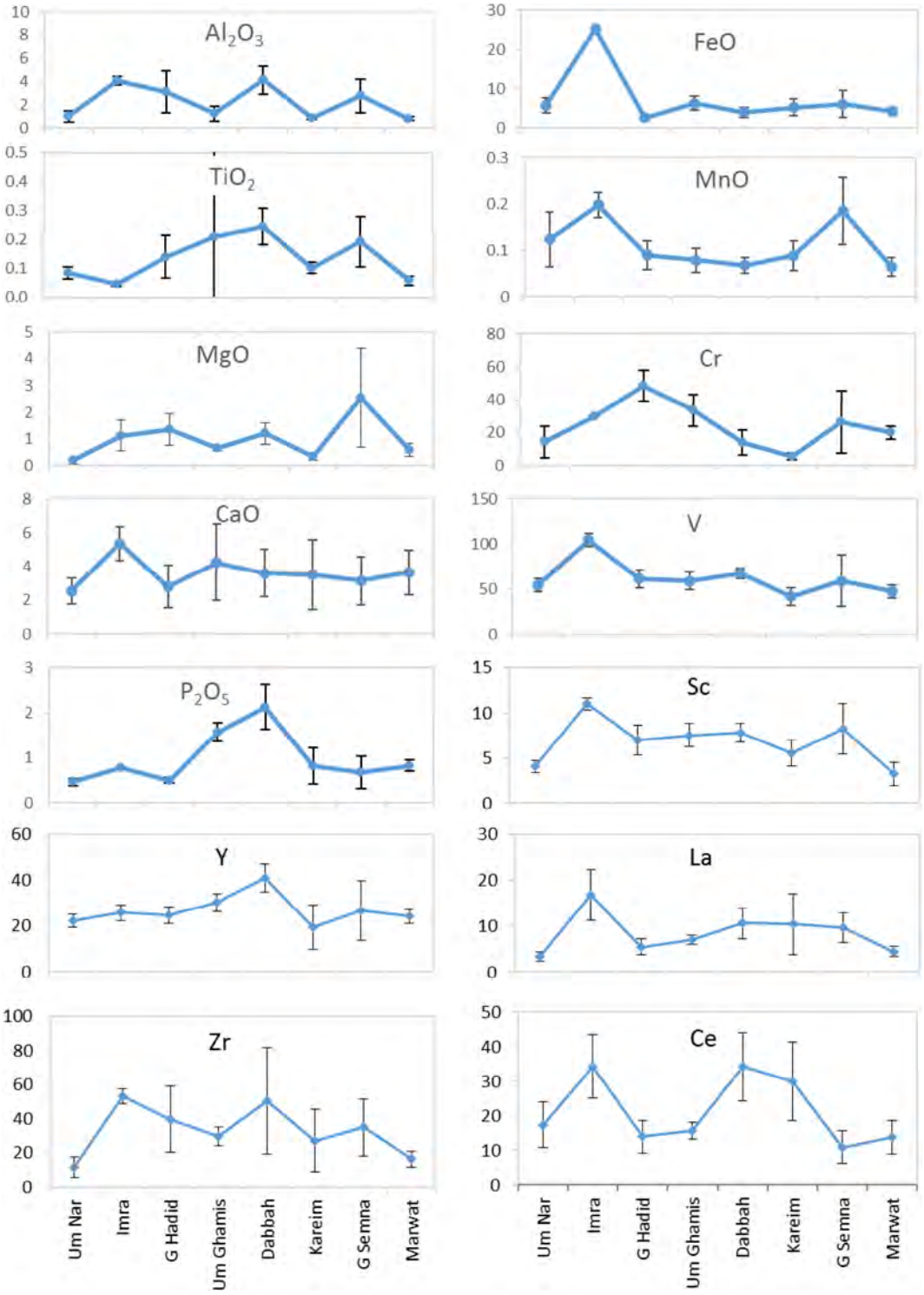

Fig. 6. Average elemental concentrations in BIFs from CED, Egypt. Deposits arranged from South (Um Nar) to Abu Marwat (North) on abscissa. Values plotted as weight % oxide for major elements, and in ppm for trace elements. Error bars represent 1 σ on each side of mean value. TiO_2 mean values plotted were calculated after elimination of samples with unusual clusters of ilmenite from Um Ghamis, although error bars are inclusive of all samples. Plots do not reflect the extreme values recorded for the ochres of Gebel Semna.

enriched, chondrite normalized REE patterns with 8–60 times relative enrichment (Supplementary Fig. 1d).

5.2.2. *Metavolcaniclastic rocks*

The metavolcaniclastic rocks are basaltic to rhyolitic in composition, with SiO_2 values of 43–75 wt% (Table 4). Because of their tuffaceous nature, they are herein plotted on chemical discriminant diagrams for metasedimentary rocks, particularly since almost all samples analyzed have compositions similar to greywackes and lithic arenites on the diagrams of Pettijohn et al. (1973) and Blatt et al. (1980). Based on their TiO_2 and Ni contents, most metavolcaniclastics have a magmatogenic signature, and also plot along the "metasediment mixing trend" on the Ni/La vs. Zr/Nb diagram of Floyd et al. (1989) (Supplementary Fig. 2a and b). On a Ce vs. Yb diagram, the samples

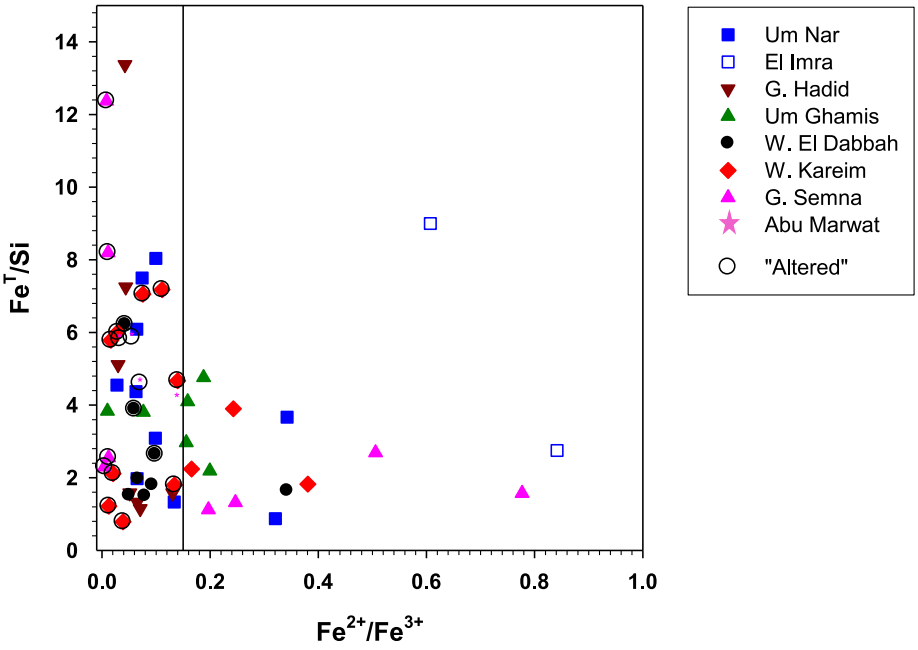

Fig. 7. Fe^T/Si vs. Fe^{2+}/Fe^{3+}. Vertical line at Fe^{2+}/Fe^{3+} = 0.15 marks the maximum value for all weathered samples (enclosed in a circle and labeled "altered").

show a clear subduction–related signature with two distinct trends: a low Ce/Yb group, and a cluster of points from Abu Marwat, Wadi Kareim and Wadi El Dabbah characterized by high Ce values (Supplementary Fig. 2c), possibly suggesting development through a thicker crust (Hawkesworth et al., 1993b).

Application of the discriminant diagrams of Bhatia (1983) and Bhatia and Crook (1986) to the metavolcaniclastics reveals that most samples fall in the oceanic island arc field (Fig. 10a & b). Using the trace element discriminant functions of Roser and Korsch (1988) reveals that almost all samples have an island arc signature (also supported by Nb and Ti troughs on NMORB normalized spider plots; Supplementary Fig. 1e), with the majority falling in the field of "immature island arc sediments" (Fig. 10c). On the other hand, chondrite normalized REE diagrams for most metavolcaniclastics are characterized by slightly LREE enriched to flat patterns with a clear negative Eu anomaly (Supplementary Fig. 1f).

6. Discussion

6.1. Chemical characteristics and element correlations for BIFs

The very high SiO_2/Al_2O_3 and low Pr/Yb ratios for all BIF samples (100–2000 and 0.4–1.12, respectively) indicate a low detrital component for the depositional basin or basins for these deposits (e.g. Yeo, 1986; Thurston et al., 2012). Plots of Y/Ho versus Zr and Y/Ho versus Pr/Yb show overall negative trends with relatively low values of Zr and Pr/Yb (Supplementary Fig. 3a and b). Because higher Zr and Pr/Yb are proxies for detrital input, such negative trends suggest a progressive dilution of detrital component with chemically precipitated BIF away from the source of detritus. Moreover, Y/Ho ratios for all samples range from 18.5 to 41 suggesting a marine hydrogenous origin influenced by hydrothermal solutions and contaminated with minor detrital sediments (Thurston et al., 2012).

A hydrothermally influenced, marine hydrogenous origin with limited detritus is also supported by plots of Al_2O_3 vs. SiO_2, Σ REE vs. Co + Cu + Ni (Supplementary Fig. 3c and d; Wonder et al., 1988; Klein and Beukes, 1993b), and Fe/Ti vs. Al/(Al + Fe + Mn) (Fig. 11a; Peter, 2003), as well as the PAAS normalized LREE depleted pattern for all deposits (Fig. 8; Klein, 2005a,b). On the other hand, variations in the REE patterns, Pr/Yb, and Y/Ho ratios from one deposit to another suggest that these BIFs were deposited in different basins as opposed to a single basin (e.g. Thurston et al., 2012). The negative Ce anomaly recorded for a few BIF samples (e.g. Gebel El Hadid, Um Ghamis, and Wadi Kareim; Fig. 8) indicates local temporal and spatial variations in the depositional environment as well as variable rates of deposition (e.g. Kato et al., 2006). The very weak positive Eu anomaly (1.02–1.7, Fig. 8) displayed by samples from Um Nar, Gebel El Hadid, and Um Ghamis also supports a hydrothermal origin for these BIFs, and suggests that the hydrothermal fluids were strongly but variably diluted by seawater (e.g. Derry and Jacobsen, 1990; Schmidt et al., 2011; Thurston et al., 2012). The variation in Eu and Ce anomalies from one sample to another within the same deposit is also a function of different BIF bands having different ages; and that no attempt has been made in this study to group BIF samples according to their relative ages.

With a hydrothermally influenced hydrogenous origin, it is tempting to use the concentrations and ratios of various trace elements (especially base metals) to infer the proximity of BIF deposition to the hydrothermal vents. However, it must first be demonstrated that some trace and major elements are indeed correlated. Various plots of some major element oxides, base metal pairs, or high field strength type elements indeed show correlations among specific pairs (Fig. 11b–d; Supplementary Fig. 4a–c). The strongest correlations are those between MnO and Sr; MgO and Al_2O_3 (Supplementary Fig. 4a and b), TiO_2 and Al_2O_3, and SiO_2 and $Fe_2O_3^T$, (Fig. 11c & d). Element or oxide pairs typically indicative of a detrital component show three trends defined by (i) Um Nar + Wadi Kareim ± Abu Marwat; (ii) Um Ghamis + Gebel El Hadid, and (iii) El Dabbah + Gebel El Hadid ± El Imra (Fig. 11b and c).

Rather than rely entirely on visual correlations, we have chosen to carry out multivariate statistical analysis of our geochemical data set by applying orthogonal R-mode factor analysis (Harman, 1976) using SPSS software. Centered log-ratio (CLR) transformation for the elemental data was carried out prior to factor analysis (Aitchison, 1986). Kaiser's (1960) criteria to extract only factor loadings with eigen values > 1 were applied. The extracted factor loadings were subjected to orthogonal rotation by the "Varimax method" to maximize the variability among all input data. The broken-stick method (Peres-Neto et al., 2003) was applied to determine which factor loading is significant. The results are summarized in Supplementary Tables 3 and 4.

Factor matrix analysis of 32 samples from the southern areas (Um

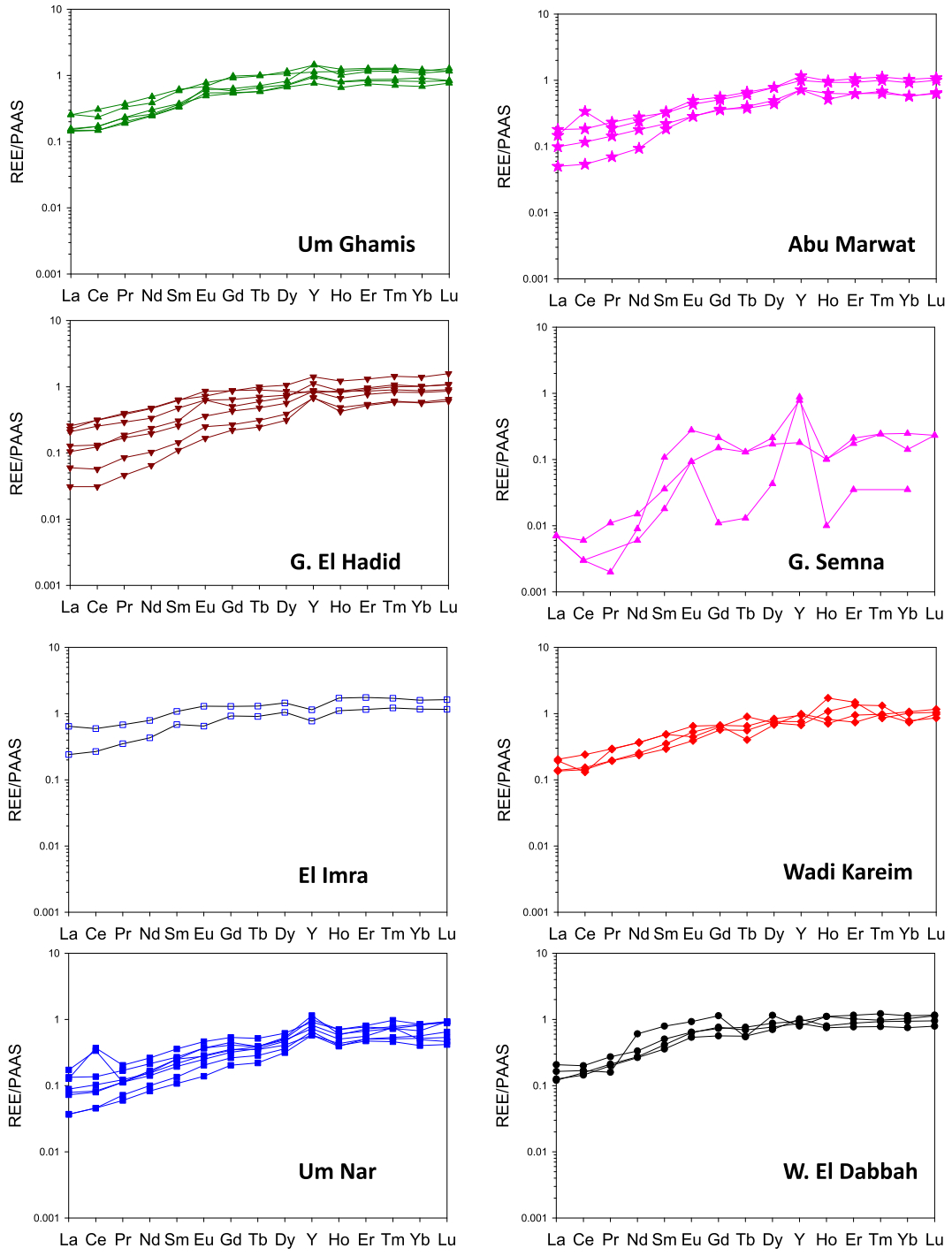

Fig. 8. REY patterns normalized to Post Archean Australian Shale (PAAS) for all BIFs investigated in this study. Altered samples from Wadi Kareim were excluded.

Nar, Gebel El Hadid, El-Imra, Um Ghamis, W. El Dabbah) results in five main factors which account for 72% of the total variance. Factor 1 represents an association of Al, Ti, Mg, Y, ± Zr. Factor 2 represents an association of Cr, Ni, and Co in which Co is antithetically correlated with the other two elements. Factor 3 (which accounts for *c.* 13% of total data variability) shows an association of Ti, Cu and P, whereas factor 4 (also accounting for *c.* 13% variability) represents an antithetic association of Si with Fe^{3+}. Factor 5 represents an association of Ca and Mn (Supplementary Table 3). Factor matrix results for 20 samples from the northern areas (i.e. W. Kariem, Abu Marwat, and Gebel Semna) are also described by five main factors that collectively account for 80.6% of the total variance. Factors 1 and 2 represent the association of Al, Ti, Mg, and Fe^{2+}, and Ca, P, Y (± Mn ± Zr), respectively. Factor 3 represents the antithetic association of Si (+Cu) with Fe^{3+}, whereas factors 4 and 5 show the positive and negative correlations between Cr and Ni, and Co and Ni, respectively (Supplementary Table 4).

Each of the factors resulting from multivariate statistical analysis should reflect some distinct geological process. Elements like Al, Zr ± Ti which appear in factor 1 are typically considered indicative of detrital material (e.g. Klein and Beukes, 1993b). The association of Mg (± Fe^{2+}) with this group of elements is likely due to weathering of arc basalts and basaltic andesites, which in turn reflects the immature nature of the associated arc. The higher % variance of factor 1 for the northern areas compared to the southern ones can be tentatively used to

Table3
Whole rock chemical analyses of metavolcanic rocks associated with the BIFs.

Sample	Um Nar			El Imra		Um Ghamis		W. El Dabbah		Wadi Kareim						Abu Marwat	
ID	N-15	N12-27	N-27	IM-1	IM-9	GH-2	GH-12	D12-6	D12-22	V1	V2	V3	K12-13	K12-27	K12-28	MW-1	MW-23
SiO_2	47.59	48.30	48.61	39.20	53.01	46.59	50.11	45.95	46.54	56.01	58.62	58.21	50.92	49.15	45.52	62.91	51.39
TiO_2	2.41	0.94	0.97	0.11	0.65	0.89	1.43	0.85	0.78	0.97	0.68	0.79	1.90	1.46	2.65	0.34	1.10
Al_2O_3	14.50	16.77	16.15	4.59	17.48	18.20	15.74	14.81	16.87	15.59	14.11	14.63	17.42	19.45	14.77	12.88	15.08
Fe_2O_{3T}	15.35	10.28	11.14	20.10	9.00	9.19	12.27	9.73	7.34	9.93	9.11	8.83	11.12	7.51	13.43	5.75	9.47
MnO	0.25	0.17	0.18	0.14	0.14	0.15	0.27	0.14	0.16	0.14	0.24	0.23	0.17	0.09	0.55	0.09	0.16
MgO	6.23	8.06	7.98	9.53	4.94	8.61	4.91	5.66	7.31	4.37	3.95	4.13	4.11	3.58	4.65	3.36	5.59
CaO	8.50	9.20	9.10	23.47	5.55	9.26	10.95	8.13	7.34	4.61	6.11	5.89	4.00	11.08	6.89	3.62	9.47
Na_2O	3.17	3.24	3.55	0.47	3.60	2.40	1.12	3.39	2.86	3.01	2.69	2.98	5.38	4.53	2.85	3.98	1.68
K_2O	0.18	0.28	0.20	0.37	0.68	1.76	0.04	0.12	0.59	0.53	0.71	0.92	0.09	0.41	0.79	0.80	0.04
P_2O_5	0.32	0.06	0.09	0.04	0.09	0.09	0.19	0.08	0.04	0.20	0.23	0.13	0.23	0.15	0.42	0.10	0.24
LOI	1.20	1.34	1.80	3.07	2.70	2.52	1.72	10.30	6.30	3.59	2.79	2.34	5.29	4.46	8.49	3.11	3.85
Totals	99.70	98.64	99.77	101.09	97.85	99.67	98.74	99.15	96.14	98.95	99.24	99.08	100.64	101.88	100.99	96.95	98.09
Ba	39.0	30.40	36.0	131.5	201	255.7	164.3	39.6	254	91.0	65.0	59.0	164.7	166.1	167.5	346	17.3
Sr	273.9	190.0	273.4	418	276	255	453	191.0	379.0	213.0	191.0	184.0	212.0	350.1	345.0	285	308
Cr	231.2	290.0	292.4	10	10	236.4	19.15	50.0	195.0	95.0	110.0	76.0	37.4	227.0	172.0	120	80
Ni	57.5	59.4	40.7	134.5	94.2	88.5	15.1	67.3	69.2	45.0	39.0	51.0	3.2	69.7	67.9	b.d.	148.0
Sc	42.0	40.8	37.0	87.0	21.0	36.6	50.1	24.0	15.9	20.0	19.0	22.0	38.0	39.4	27.0	16	33.0
V	443.0	322.5	b.d.	19.0	b.d.	217.0	282.0	293.5	285.0	225.0	240.0	231.0	276.4	175.6	281.0	171.0	326.0
Nb	3.5	2.0	0.7	0.9	2.6	6.6	8.2	4.2	11.5	7.0	7.0	10.0	12.4	10.6	19.4	4.2	3.8
Y	35.5	21.8	23.5	16.9	13.6	16.6	26.8	21.1	25.0	31.0	24.0	21.0	40.4	25.3	39.5	10.1	19
Zr	141.8	124.8	68	34	52	85.0	52.1	60.0	45.6	50.0	85.0	54.0	129.8	99.2	259.3	79	44
Hf	4	1.9	1.8	1	1.7	b.d.	b.d.	1.8	b.d.	n.d.	n.d.	n.d.	b.d.	b.d.	0.8	2.3	1.4
Th	0.6	0.2	0.1	0.3	0.4	11.0	9.5	0.8	2.6	n.d.	n.d.	n.d.	7.4	5.2	13.8	3.2	6.9
La	7.3	8.7	2.1	2.6	7.5	14.0	29.5	6.2	16.5	n.d.	n.d.	n.d.	13.0	18.0	48.9	13.6	3.1
Ce	22.5	5.8	7.7	5.7	16.8	57.4	30.7	13.2	39.5	n.d.	n.d.	n.d.	8.1	7.6	48.0	27	7.9
Pr	3.34	1.1	1.26	0.83	2.07	n.d.	n.d.	1.7	n.d.	n.d.	n.d.	n.d.	n.d.	n.d.	n.d.	3.19	1.27
Nd	16.8	6.8	7.4	4.1	9.3	n.d.	n.d.	8.7	n.d.	n.d.	n.d.	n.d.	n.d.	n.d.	n.d.	13.2	6.8
Sm	4.83	2.3	2.45	1.21	2.34	n.d.	n.d.	2.4	n.d.	n.d.	n.d.	n.d.	n.d.	n.d.	n.d.	2.64	2.26
Eu	1.84	0.9	0.93	0.31	0.72	n.d.	n.d.	0.9	n.d.	n.d.	n.d.	n.d.	n.d.	n.d.	n.d.	0.73	0.94
Gd	6.12	3.3	3.56	1.55	2.4	n.d.	n.d.	3.4	n.d.	n.d.	n.d.	n.d.	n.d.	n.d.	n.d.	2.18	3.04
Tb	1.04	0.6	0.61	0.3	0.4	n.d.	n.d.	0.5	n.d.	n.d.	n.d.	n.d.	n.d.	n.d.	n.d.	0.33	0.54
Dy	6.37	3.7	3.93	2.06	2.54	n.d.	n.d.	3.6	n.d.	n.d.	n.d.	n.d.	n.d.	n.d.	n.d.	1.83	3.47
Ho	1.32	0.8	0.87	0.5	0.54	n.d.	n.d.	0.8	n.d.	n.d.	n.d.	n.d.	n.d.	n.d.	n.d.	0.38	0.77
Er	3.83	2.4	2.54	1.47	1.52	n.d.	n.d.	2.3	n.d.	n.d.	n.d.	n.d.	n.d.	n.d.	n.d.	1.08	2.14
Tm	0.53	0.4	0.35	0.23	0.23	n.d.	n.d.	0.3	n.d.	n.d.	n.d.	n.d.	n.d.	n.d.	n.d.	0.17	0.35
Yb	3.45	2.4	2.46	1.49	1.46	2.2	b.d.	2.2	2.7	n.d.	n.d.	n.d.	1.7	3.2	4.5	1.03	2.08
Lu	0.52	0.3	0.37	0.23	0.23	b.d.	b.d.	0.3	0.5	n.d.	n.d.	n.d.	0.8	0.8	0.8	0.17	0.31

Major element oxides in weight %, trace elements in ppm. b.d.: below detection; n.d. not determined.

suggest closer proximity of the northern basins to the arc from which the detrital material was derived. The strong negative correlation between Fe^{3+} and Si (demonstrated by factors 4 and 3 for the southern and northern areas, respectively) is clearly an artefact of the constant sum effect, as plots of the ratios $Fe_2O_3{}^T/Al_2O_3$ vs. SiO_2/Al_2O_3 show a clear positive correlation (Fig. 11d) with some similarity to the three trends observed for other element pairs (e.g. Fig. 11b–c).

Both Fe and Si ± Cu (as well as Co, Zn, and Pb) are hydrothermal in origin and chemically precipitated either simultaneously or sequentially (e.g. Morris, 1993; Ohmoto et al., 1996). The association of Cr and Ni as rotated factors 4 and 2 (Supplementary Tables 3 and 4) most probably reflects alteration of ocean floor mafic and ultramafic rocks. The association of Ca, Mn ± P ± Y (and likely Sr which was not included in the factor matrix analysis) reflects the chemical precipitation of minor carbonates and apatite. On the other hand, the three trends observed on the correlation diagrams of Fig. 11 may be explained by either (i) three different volcanic pulses which provided ash compositionally ranging from basaltic to andesitic (Table 4), as suggested by geochronological results of El-Shazly and Khalil (2016); or (ii) some BIF samples affected by variable degrees of hydrothermal alteration, Ca metasomatism, or weathering.

6.2. Proximity of BIF deposition to submarine vents

The previous discussion demonstrates that all BIFs have a marine hydrogenous origin influenced by hydrothermal solutions with some detrital component, and that not all CED BIFs formed in the same basin. It is therefore safe to assume that both Fe and SiO_2 have a hydrothermal origin. Nevertheless, the very low concentration of Cu, Co, Zn (typically deposited at T > 250 °C, e.g. Klein, 2005a,b; Ohmoto et al., 2006) suggests that the BIFs were all deposited in a distal location relative to the submarine hydrothermal vents at temperatures below 200 °C. This conclusion is also supported by the paucity of sulfide facies, as well as the lack of, or very weak positive Eu anomaly displayed by most deposits, as higher Eu/Eu* values are indicative of a stronger hydrothermal influence, which is more enhanced closest to the vents (Derry and Jacobsen, 1990; Thurston et al., 2012; Cox et al., 2013).

Relative proximity of each deposit to its respective hydrothermal vent can also be surmised from the size of the deposit (larger deposits like Um Nar located closer to the hydrothermal source), and the relative amounts of detrital components in each BIF, as deeper marine BIFs (which form closer to their vents) receive fewer detrital material. Other criteria for establishing proximity to hydrothermal vents/ depth of deposition include: (i) the relative abundance of chert bands and jaspilites in BIFs; deposits forming closer to the vents are more enriched in chert (e.g. Beukes and Gutzmer, 2008), and (ii) the presence of a granular/ pisolitic texture in BIFs which develops in shallow marine environments away from hydrothermal vents (Beukes and Gutzmer, 2008), (iii) Y/Ho ratios which increase then decrease away from vents (Thurston et al., 2012); and (iv) Pr/Yb ratios which increase with increased detrital material at shallower depths of deposition (Thurston et al., 2012).

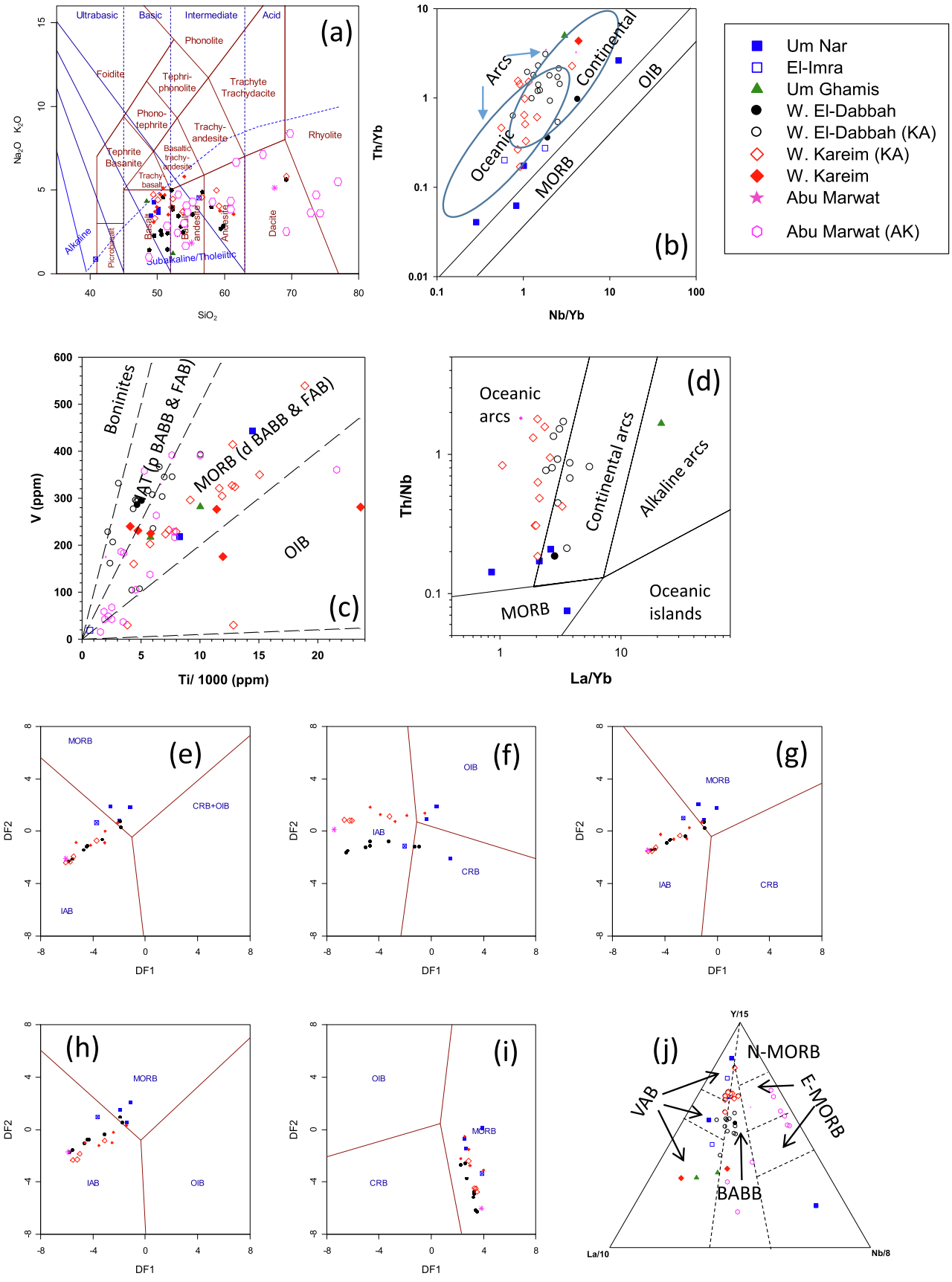

Fig. 9. Chemical characterization of metavolcanic rocks associated with the BIF. (a) Total alkali vs. SiO_2 diagram for the classification of all metavolcanic rocks after Le Bas et al. (1986). (b) Th/Yb vs. Nb/Yb diagram of Pearce (2008, 2014). (c) Ti vs. V diagram of Shervais (1982). (d) Th/Nb vs. La/Yb discriminant diagram of Hollocher et al. (2012). (e)–(i) Trace element discriminant functions (DF1 and DF2) of Agrawal et al. (2008) for metabasaltic samples. (j) Y–La–Nb diagram of Cabanis and Lecolle (1989) for metabasaltic samples. KA: data from Ali et al. (2009); AK: data from Mohamed Abdel Kareem (2018; pers. Comm).

Table 4
Whole rock chemical compositions of Metavolcaniclastic rocks hosting the BIFs.

	Um Nar								El Imra	G. Hadid						Um Ghamis			
Sample	N-17	N12-18	N12-6	N12-51	N12-19	N12-46	N12-47	N-32	IM-9	H-4	H-14	H-19	H-40	H-6	H-28	GH-26	GH-27	GH-28	GH-29
SiO_2	57.43	53.46	53.84	67.40	63.16	63.76	68.99	66.32	53.01	43.39	46.79	45.55	37.63	60.51	51.84	56.26	64.36	62.21	59.38
TiO_2	0.67	0.45	1.12	0.73	0.32	0.63	0.50	0.63	0.65	2.54	2.46	2.33	0.94	0.73	0.50	0.51	0.56	0.64	0.53
Al_2O_3	16.86	12.23	16.44	13.71	14.95	13.60	12.85	13.13	17.48	13.21	12.50	13.48	10.56	13.55	16.24	10.94	12.27	12.66	12.12
Fe_2O_{3T}	8.19	9.17	10.89	6.32	6.97	6.95	4.81	7.16	9.00	14.98	14.32	12.98	7.17	6.27	8.61	20.54	6.43	6.18	15.77
MnO	0.16	0.20	0.20	0.10	0.15	0.11	0.10	0.11	0.14	0.19	0.22	0.21	0.11	0.11	0.14	0.11	0.13	0.14	0.09
MgO	3.95	6.89	4.90	1.64	4.50	3.61	1.31	1.88	4.94	5.27	4.47	4.45	9.37	2.30	5.06	2.20	1.86	2.08	1.86
CaO	4.02	15.23	6.79	4.19	6.31	3.01	3.30	5.63	5.55	7.21	9.23	8.17	13.87	4.90	6.43	3.21	6.43	6.18	2.91
Na_2O	5.02	0.94	5.23	4.84	3.39	3.98	5.31	3.43	3.60	3.27	2.71	3.74	2.27	4.19	3.83	2.00	2.94	2.51	0.73
K_2O	1.16	0.55	0.29	0.26	0.57	0.11	0.26	0.40	0.68	0.04	0.06	0.04	0.04	0.68	0.55	2.18	0.17	0.73	3.15
P_2O_5	0.13	0.06	0.18	0.21	0.05	0.15	0.12	0.12	0.09	0.29	0.29	0.31	0.13	0.13	0.11	0.59	0.45	0.11	1.03
LOI	2.20	1.10	1.16	0.74	1.37	2.29	0.87	1.00	2.70	9.40	6.70	8.50	17.70	6.50	6.50	1.34	0.99	2.15	1.90
Totals	99.79	100.28	101.04	100.14	101.74	98.20	98.42	99.81	97.85	99.79	99.75	99.76	99.79	99.87	99.81	99.87	96.59	95.58	99.47
Ba	186	78	146	60	125	211	77	119	201	37	29	37	21	210	230	90	205	627	116
Sr	468	113	399	285	173	194	192	273	276	264	430	481	174	174	235	385	314	291	117
Cr	210.8	510.0	120.6	25.0	44.0	150.0	17.2	95.2	10.0	160.0	140.0	100.0	90.0	90.0	210.0	23.6	10.0	20.0	23.0
Ni	47.1	75.9	45.8	18.8	42.6	23.9	37.2	38.7	94.2	49.8	44.2	34.4	22.7	21.3	70.1	215.0	b.d.	80.5	26.9
Sc	26.0	52.1	35.9	22.0	25.1	27.6	27.8	18.0	21.0	42.0	41.0	39.0	24.0	19.0	28.0	19.0	19.0	25.0	17.4
V	194.0	472.5	275.5	137.0	145.4	133.0	69.0	167.0	277.0	435.0	460.0	404.0	145.0	112.0	220.0	80.0	89.0	102.0	75.0
Nb	1.8	4.6	18.8	12.7	b.d.	13.2	13.2	3.1	2.6	5.1	5.2	5.1	2.2	4.9	1.7	b.d.	7.7	5.6	b.d.
Y	18.8	7.1	15.7	34.9	21.9	25.5	10.7	27.1	13.6	35.9	38.7	37.4	18.9	30.1	11.3	95.7	32.0	34.8	30.7
Zr	72.2	55.0	135.4	149.0	64.2	133.5	141.5	137.2	52.0	137.4	150.6	154.4	67.1	144.0	42.5	72.0	149.0	145.0	141.0
Hf	1.9	0.6	b.d.	4.5	b.d.	4.4	n.d.	3.8	1.7	3.5	3.9	4.1	2.2	4.0	1.3	b.d.	4.3	4.2	b.d.
Th	1.1	0.3	6.0	2.5	1.0	4.1	2.0	2.0	0.4	0.5	0.6	0.7	0.5	3.3	1.4	6.8	2.5	2.2	5.4
La	8.2	6.2	9.1	9.9	8.3	13.6	10.1	9.5	7.5	6.8	8.1	8.4	5.7	11.6	8.8	16.8	14.0	13.1	18.9
Ce	16.7	7.6	6.7	27.5	10.9	36.5	39.2	24.6	16.8	20.3	23.4	24.6	14.8	28.5	19.7	22.0	30.3	28.2	45.7
Pr	2.26	1.05	n.d.	3.36	n.d.	3.72	n.d.	3.29	2.07	3.08	3.58	3.61	2.10	3.71	2.36	n.d.	3.98	3.76	n.d.
Nd	10.5	5.3	n.d.	14.5	n.d.	16.9	n.d.	15.5	9.3	16.0	17.8	19.3	10.8	16.9	10.1	n.d.	18.6	18.1	n.d.
Sm	2.66	1.27	n.d.	4.21	n.d.	3.71	n.d.	3.86	2.34	4.78	5.13	5.12	2.83	4.01	2.00	n.d.	4.51	4.49	n.d.
Eu	0.94	0.43	n.d.	1.18	n.d.	1.00	n.d.	1.26	0.72	1.78	1.87	1.77	0.89	1.04	0.64	n.d.	1.09	1.22	n.d.
Gd	2.99	1.37	n.d.	4.93	n.d.	3.86	n.d.	4.48	2.40	6.18	6.51	6.51	3.43	4.57	1.93	n.d.	5.02	5.23	n.d.
Tb	0.49	0.20	n.d.	0.84	n.d.	0.61	n.d.	0.78	0.40	1.07	1.14	1.14	0.57	0.83	0.33	n.d.	0.81	0.85	n.d.
Dy	3.04	1.30	n.d.	5.69	n.d.	4.15	n.d.	4.54	2.54	6.58	6.76	6.72	3.44	5.00	1.95	n.d.	5.33	5.74	n.d.
Ho	0.62	0.26	n.d.	1.18	n.d.	0.91	n.d.	0.98	0.54	1.38	1.44	1.45	0.75	1.09	0.40	n.d.	1.11	1.21	n.d.
Er	1.87	0.81	n.d.	3.71	n.d.	2.83	n.d.	2.83	1.52	3.90	4.25	4.12	2.14	3.25	1.18	n.d.	3.39	3.71	n.d.
Tm	0.27	0.12	n.d.	0.57	n.d.	0.46	n.d.	0.46	0.23	0.58	0.62	0.58	0.32	0.49	0.19	n.d.	0.53	0.57	n.d.
Yb	1.96	0.75	2.66	3.64	b.d.	3.18	3.02	3.04	1.46	3.58	3.96	3.75	2.05	3.28	1.22	5.10	3.62	3.90	4.60
Lu	0.30	0.11	b.d.	0.59	b.d.	0.47	b.d.	0.44	0.23	0.54	0.60	0.57	0.31	0.51	0.18	0.24	0.53	0.58	0.36

	W. El Dabbah										W. Kareim						Abu Marwat	
Sample	D12-7	DB-121	DB-148	DB-133	DB-137	DB-117	DB-141	DB-150	DB-133b	D23	K-2	K-3	K-28	WK-S1	K-26	K-27	MW-19	MW-22
SiO_2	61.51	64.20	63.50	64.30	62.60	59.72	60.93	61.74	64.64	47.43	68.70	67.10	61.10	63.05	60.99	59.00	57.98	56.21
TiO_2	0.90	0.64	0.68	0.66	0.70	0.73	0.54	0.60	0.47	1.58	0.58	0.61	0.71	0.62	0.73	0.91	0.94	0.756
Al_2O_3	13.33	13.90	13.80	13.00	14.30	14.74	9.97	13.41	5.03	15.21	11.50	12.50	12.90	11.71	13.53	11.60	15.58	13.19
Fe_2O_{3T}	6.11	8.00	9.92	9.05	8.60	10.11	9.00	9.00	9.00	13.73	7.17	6.72	8.15	8.16	7.71	8.21	8.62	9.47
MnO	0.04	0.08	0.11	0.08	0.11	0.51	0.13	0.07	0.08	0.18	0.06	0.09	0.13	0.31	0.25	0.13	0.15	0.09
MgO	1.23	1.23	1.39	2.50	1.41	1.51	4.39	2.14	2.91	6.95	2.16	2.43	4.46	3.69	3.25	4.82	4.38	2.67
CaO	3.32	6.39	4.80	4.48	5.61	6.50	4.50	3.51	5.00	11.51	2.07	3.11	5.03	4.78	6.11	5.90	2.25	6.04
Na_2O	3.54	1.47	1.83	2.29	1.69	1.17	3.55	2.20	2.11	2.26	1.64	2.64	2.43	3.31	2.91	2.46	5.25	2.22
K_2O	5.45	2.16	1.80	1.37	1.43	1.26	0.16	2.47	1.30	0.38	1.37	1.84	0.20	0.68	0.52	2.84	0.35	1.74
P_2O_5	0.07	0.15	0.14	0.63	0.42	0.19	2.35	1.02	1.47	0.10	0.13	0.17	0.13	0.22	1.15	0.14	0.78	0.87
LOI	6.80	1.99	1.80	1.78	1.81	2.61	1.21	1.64	2.25	2.38	3.90	2.55	5.22	3.01	3.81	3.10	3.09	7.8
Totals	102.31	100.21	99.77	100.14	98.68	99.05	96.73	97.80	94.26	101.71	99.28	99.76	100.46	99.54	100.96	99.11	99.37	101.06
Ba	600	481	292	242	323	311	121	n.d.	n.d.	117	220	107	38	45	68	308	30	173
Sr	35	n.d.	n.d.	n.d.	n.d.	n.d.	74	n.d.	n.d.	343	106	166	142	161	148	180	175	200
Cr	370.0	53.0	40.0	84.0	60.0	51.0	46.0	n.d.	n.d.	89.4	51.0	39.0	46.0	41.0	51.0	58.0	b.d.	47.8
Ni	b.d.	21.0	32.0	28.0	21.0	24.0	12.0	n.d.	n.d.	38.8	34.0	45.0	41.0	29.0	39.0	25.0	b.d.	30.5
Sc	33.0	22.0	19.0	21.0	20.0	n.d.	10.0	14.0	6.0	49.1	12.0	17.0	19.0	21.0	26.0	15.0	34.0	20.0
V	290.5	94.0	102.0	85.0	96.0	n.d.	69.0	80.0	71.0	742.0	98.0	146.0	134.0	125.0	111.0	108.0	145.0	99.7
Nb	0.9	16.0	12.0	14.0	12.0	13.0	6.0	n.d.	n.d.	3.9	5.0	7.0	6.0	5.0	5.0	7.0	12.3	11.2
Y	21.9	2.5	6.0	2.5	2.5	2.5	21.6	n.d.	n.d.	18.8	16.0	19.0	25.0	14.0	21.0	29.0	23.2	24.7
Zr	88.0	138.0	143.0	110.0	134.0	n.d.	243.2	126.0	56.0	62.3	93.0	101.0	126.0	91.0	125.0	113.0	109.4	178.0
Hf	2.3	n.d.	n.d.	n.d.	n.d.	n.d.	6.6	n.d.	n.d.	1.4	n.d.	n.d.	n.d.	n.d.	8.3	n.d.	b.d.	0.2
Th	0.1	n.d.	n.d.	n.d.	n.d.	n.d.	286.0	n.d.	n.d.	3.7	b.d.	n.d.	2.9	n.d.	3.5	b.d.	4.1	8.9
La	1.9	33.0	35.0	40.0	43.0	36.0	9.0	n.d.	n.d.	5.9	b.d.	n.d.	27.6	n.d.	51.1	b.d.	38.0	31.6
Ce	7.0	n.d.	n.d.	n.d.	n.d.	n.d.	54.3	n.d.	n.d.	16.5	b.d.	n.d.	60.0	n.d.	58.2	b.d.	47.0	64.1
Pr	1.22	n.d.	n.d.	n.d.	n.d.	n.d.	n.d.	n.d.	n.d.	1.78	n.d.	n.d.	n.d.	n.d.	n.d.	n.d.	n.d.	n.d.
Nd	7.8	n.d.	n.d.	n.d.	n.d.	n.d.	n.d.	n.d.	n.d.	8.4	n.d.	n.d.	n.d.	n.d.	n.d.	n.d.	n.d.	n.d.
Sm	2.80	n.d.	n.d.	n.d.	n.d.	n.d.	n.d.	n.d.	n.d.	2.37	n.d.	n.d.	n.d.	n.d.	n.d.	n.d.	n.d.	n.d.
Eu	0.63	n.d.	n.d.	n.d.	n.d.	n.d.	n.d.	n.d.	n.d.	0.94	n.d.	n.d.	n.d.	n.d.	n.d.	n.d.	n.d.	n.d.

(*continued on next page*)

Table 4 (*continued*)

	W. El Dabbah										W. Kareim						Abu Marwat	
Sample	D12-7	DB-121	DB-148	DB-133	DB-137	DB-117	DB-141	DB-150	DB-133b	D23	K-2	K-3	K-28	WK-S1	K-26	K-27	MW-19	MW-22
Gd	3.84	n.d.	n.d.	n.d.	n.d.	n.d.	n.d.	n.d.	n.d.	3.08	n.d.	n.d.	n.d.	n.d.	n.d.	n.d.	n.d.	n.d.
Tb	0.62	n.d.	n.d.	n.d.	n.d.	n.d.	n.d.	n.d.	n.d.	0.53	n.d.	n.d.	n.d.	n.d.	n.d.	n.d.	n.d.	n.d.
Dy	4.16	n.d.	n.d.	n.d.	n.d.	n.d.	n.d.	n.d.	n.d.	3.47	n.d.	n.d.	n.d.	n.d.	n.d.	n.d.	n.d.	n.d.
Ho	0.89	n.d.	n.d.	n.d.	n.d.	n.d.	n.d.	n.d.	n.d.	0.74	n.d.	n.d.	n.d.	n.d.	n.d.	n.d.	n.d.	n.d.
Er	2.71	n.d.	n.d.	n.d.	n.d.	n.d.	n.d.	n.d.	n.d.	2.01	n.d.	n.d.	n.d.	n.d.	n.d.	n.d.	n.d.	n.d.
Tm	0.41	n.d.	n.d.	n.d.	n.d.	n.d.	n.d.	n.d.	n.d.	0.31	n.d.	n.d.	n.d.	n.d.	n.d.	n.d.	n.d.	n.d.
Yb	2.72	n.d.	n.d.	n.d.	n.d.	n.d.	1.63	n.d.	n.d.	1.97	0.27	n.d.	b.d.	n.d.	2.00	0.46	3.10	3.60
Lu	3.90	n.d.	n.d.	n.d.	n.d.	n.d.	0.14	n.d.	n.d.	0.29	n.d.	n.d.	n.d.	n.d.	0.55	n.d.	0.65	0.72

Major element oxides in weight %, trace elements in ppm. b.d.: below detection; n.d. not determined.

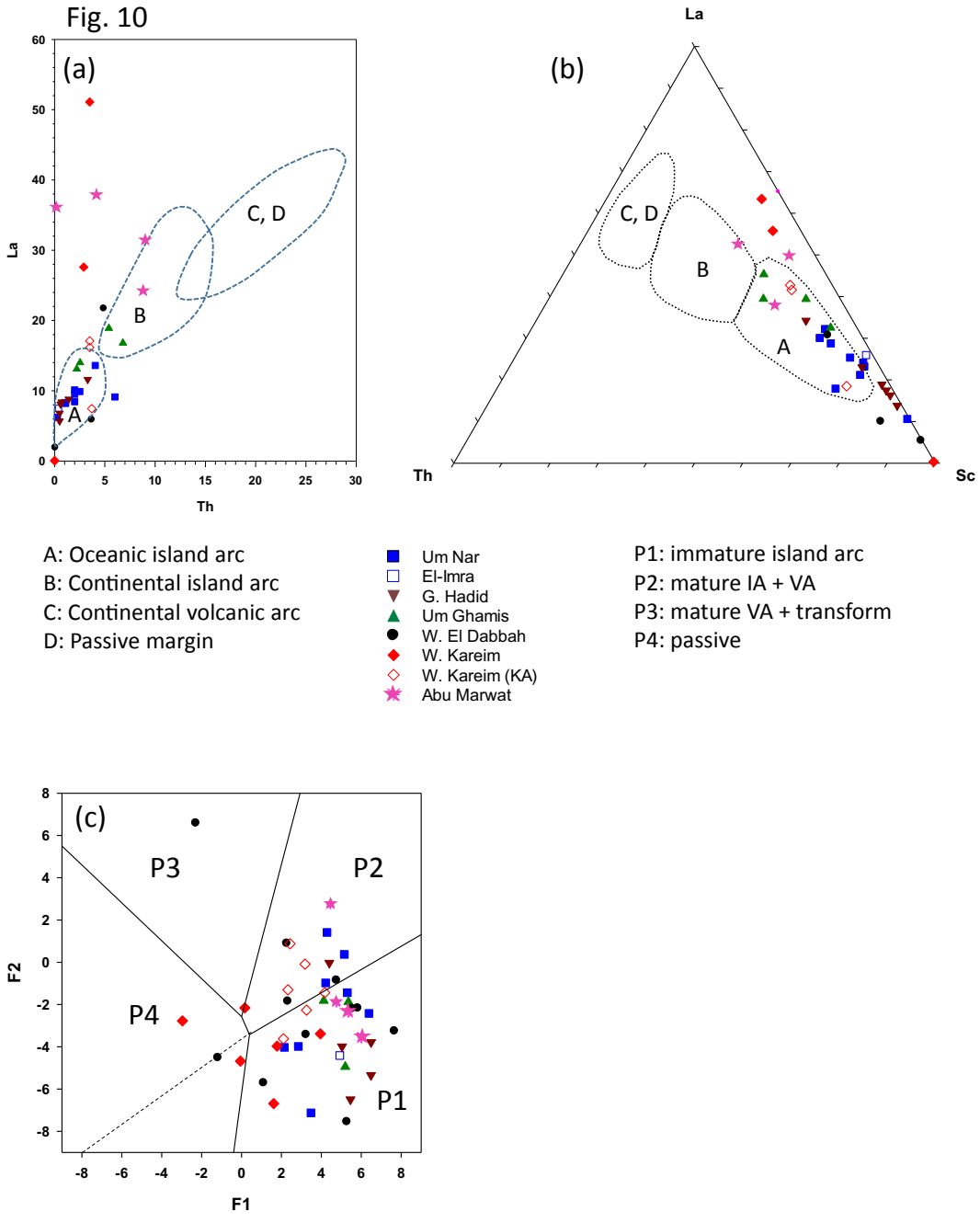

Fig. 10. Discriminant diagrams for metavolcaniclastics. (a) and (b) La vs. Th and La–Th–Sc ternary of Bathia and Crook (1986). (c) Trace element discriminant functions (F1 and F2) and diagram of Roser and Korsch (1988).

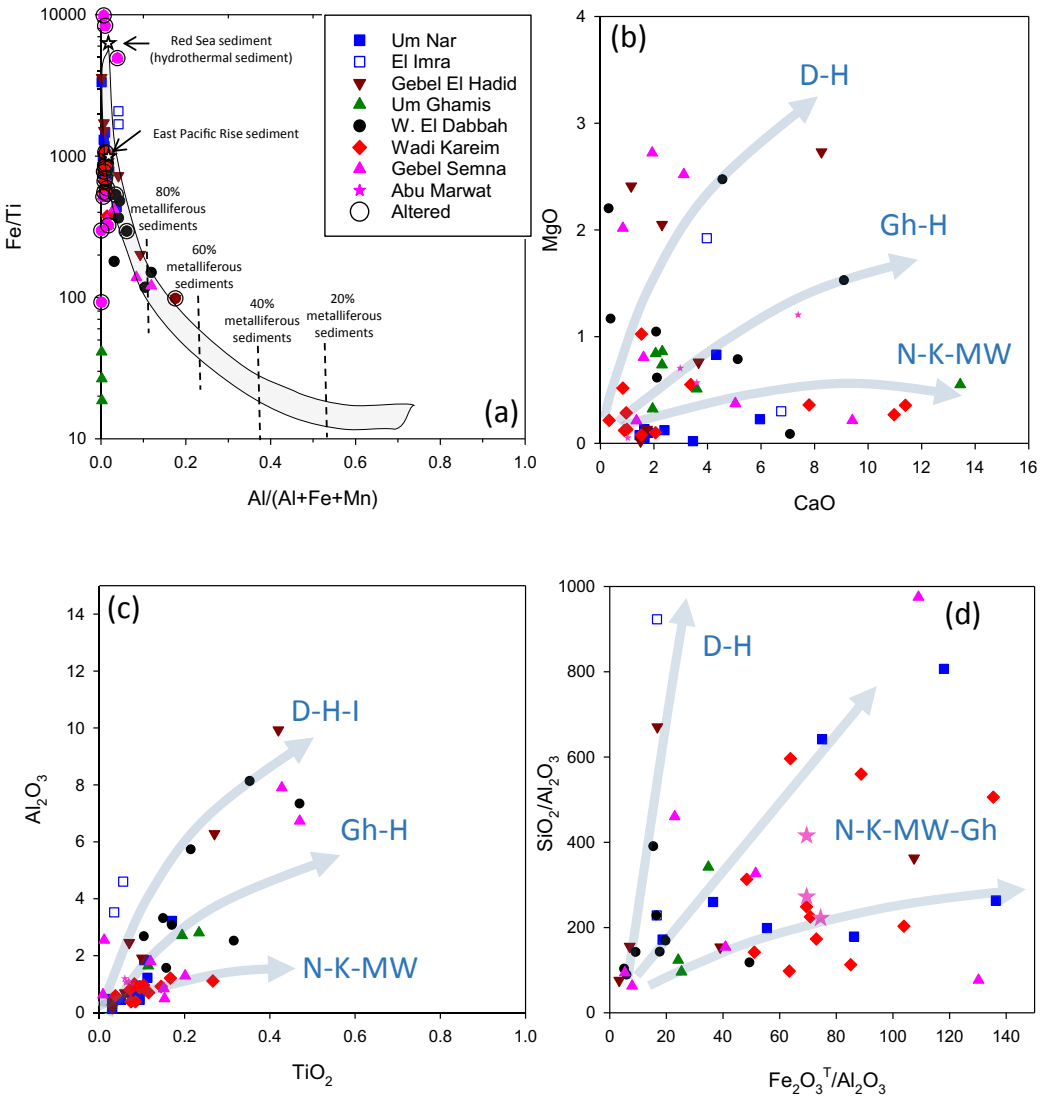

Fig. 11. (a) Fe/Ti vs. Al/(Al + Fe + Mn) of Peter (2003). (b)–(d) Correlation diagrams for various oxides/ ratios for all BIF samples. Arrows suggest possible correlation trends: D: Wadi El Dabbah, H: Gebel El Hadid; I: El Imra, Gh: Um Ghamis, N: Um Nar, K: Wadi Kareim; MW: Abu Marwat. Note that whereas elements attributed to a detrital component yield 3 trends defined by the same deposits, trends for chemically precipitated SiO_2 and Fe_2O_3 are different.

Petrographically, BIFs from Wadi El Dabbah are characterized by the highest detrital component, where lithic fragments and fiamme occur interlaminated with magnetite and hematite (El-Shazly et al., 2011). The distal nature of Wadi El Dabbah is also supported by the abundance of fine-grained magnetite I (Fig. 4b) interpreted by many as a replacement of finer-grained Fe-oxyhydroxides away from the submarine vents (e.g. Lobato et al., 2008). The geochemical trends of Fig. 6 where Wadi El Dabbah BIFs show the highest concentrations of Al_2O_3, TiO_2, Zr, and Y; oxides and elements indicative of detrital material, also support a distal location from hydrothermal vents (corresponding to a more proximal location to land masses). On the other hand, jaspilites are more abundant in Wadi Kareim and Um Nar (Fig. 3c and d), whereas only BIFs from Abu Marwat show a pisolitic texture (Fig. 3e & g). Average Y/Ho ratios for each BIF are generally highest for Um Nar and Gebel El Hadid, and decrease towards Wadi El Dabbah, El Imra, and Wadi Kareim. On the other hand, average Pr/Yb ratios exhibit a systematic increase from Um Nar and Gebel El Hadid to the south and Abu Marwat to the north towards Wadi El Dabbah which records the highest Pr/Yb values (Table 2). A plot of Y/Ho vs. Pr/Yb shows negative trends defined by most deposits except those of El Imra and Wadi Kareim (Supplementary Fig. 3b). We therefore conclude that deposition of these BIFs occurred in discrete basins with Wadi El Dabbah occurring closest to an active island arc that provided it with the largest amount of detritus, whereas Um Nar and Gebel El Hadid were located closest to their submarine vents. On the other hand, the BIF of Abu Marwat formed in a shallow marine environment that did not receive much detrital material, whereas El Imra and other small BIFs in the north (e.g. Um Anab; Basta et al., 2011) seem to have been located relatively close to a detrital source but at a significant distance from hydrothermal vents.

6.3. *Effects of hydrothermal alteration and weathering on BIFs*

Many samples from various BIFs were variably affected by hydrothermal alteration and/ or weathering. Hydrothermal alteration in the form of an intricate network of calcite veins is most obvious in Wadi Kareim which is located on a large shear zone. Other deposits affected by hydrothermal alteration include El Imra, Um Ghamis, and Wadi El Dabbah, where veins of andradite–rich garnet and/ or calcite cross cut the iron ore. Weathering on the other hand is indicated by the relative abundance of goethite and lepidocrocite in BIFs; both phases identified by reflected light microscopy. Hydrothermal alteration may have

played a role in increasing the Fe/Si ratio of the BIFs from ca. 1.2 (average Algoma deposits; Gross and McLeod, 1980) to as much as 5–8 (Table 2; Khalil and El-Shazly, 2012). The observation that many altered BIFs occur close to serpentinites led El-Shazly and Khalil (2014, 2016) to suggest that Ca metasomatism related to serpentinization of ultramafic bodies may have leached silica from nearby BIFs hence increasing their Fe/Si ratios.

To test this hypothesis, and investigate the effects of hydrothermal alteration we plot CaO/Al_2O_3 vs. Fe_2O_3/Al_2O_3, (Supplementary Fig. 4d) and CaO/TiO_2 vs. Fe_2O_3/TiO_2. These pairs were selected because hydrothermal alteration is always associated with the formation of Ca rich phases as andradite, epidote, or calcite, whereas Ca itself was not chemically precipitated with SiO_2 and Fe_2O_3 as demonstrated by the results of factor analysis discussed above. Plotting ratios instead of direct oxides was done to overcome the constant sum effects expected by the very high concentration of Fe_2O_3 in BIFs. These plots show positive trends for BIFs from Gebel El Hadid, Um Ghamis, and Gebel Semna (with R^2 values of 0.68–0.9), but no correlations for samples from Wadi Kareim, Wadi El Dabbah, Um Nar, or Abu Marwat (Supplementary Fig. 4d). Given that Wadi Kareim and Abu Marwat BIFs are the ones most affected by hydrothermal alteration, we conclude that Ca metasomatism or hydrothermal alteration was not necessarily associated with an increase in $Fe_2O_3^T$. Moreover, serpentinization releases Ca-rich and Mg-poor fluids. If such fluids were to hydrothermally alter the BIFs, CaO and MgO would be expected to display a negative correlation in these rocks. Instead, CaO and MgO are positively correlated (Fig. 11b), displaying the “three trends” typical of most oxides indicative of a detrital origin (e.g. Fig. 11c; Supplementary Fig. 4b).

Weathering is expected to decrease the Fe^{2+}/Fe^{3+} ratio for all BIFs. Weathering may also leach most other elements and oxides including silica. This will ultimately increase the total Fe content of the BIFs. A plot of Fe^{2+}/Fe^{3+} vs. Fe^T/Si for all samples affected by weathering is therefore expected to display a clear negative trend. However, weathered samples display a wide range of Fe^T/Si values (Fig. 7). This suggests that processes other than chemical weathering played a significant role in controlling the Fe^T/Si ratios. Nevertheless, extensive weathering has definitely resulted in a spectacular increase in the concentration of some elements like V, Cr, Cu and Zn as demonstrated by the ochers of Gebel Semna (Table 2), and an overall decrease in REE concentrations (Fig. 8; Table 2).

6.4. Tectonic setting of the host rocks

Chemical characteristics of the rocks hosting all BIFs and the tectonic discrimination diagrams and NMORB normalized spider plots of Figs. 9 and 10, and Supplementary Fig. 1c–f show that metavolcanic and metavolcaniclastic rocks have an arc signature. Most samples plot as island arc basalts, although samples from Um Nar plot either close to or within the fields of MORB (Fig. 9b–d). Discriminant functions of Roser and Korsch (1988) suggest that the arc was mostly immature (Fig. 10c). Plots of Ti vs. V (Shervais, 1982) show samples from Um Nar, El Imra, Um Ghamis, Wadi Kareim, and Abu Marwat plotting as “slab-distal” back- or fore-arc basin MORBs, whereas almost all samples from Wadi El Dabbah fall in the IAT/ “slab-proximal” back- or fore- arc basin basalt fields (Fig. 9c). Despite the difficulty in using geochemical data for further discrimination, it is worth noting that data points from Wadi Kareim, Gebel El Hadid, and Wadi El Dabbah cluster in the field of back-arc basins as defined by Hollocher et al. (2012) and Cabanis and Lecolle (1989) (Fig. 9d and j).

Combining these results with the previous discussion on the BIFs, we conclude that Wadi El Dabbah represented the location of an immature oceanic island arc, with a back arc basin in which BIFs of Um Nar, Gebel El Hadid, and Um Ghamis were deposited in a progressively more distal location relative to the submarine hydrothermal vent (i.e. progressively closer to the arc). Wadi El Dabbah BIF must have been deposited in a shallow silled basin bordering the island arc, whereas El Imra may have been deposited in a small intra-arc basin, which would explain their highest content of detrital material and lowest amount of chert among all deposits. BIFs to the north of Wadi El Dabbah were likely deposited in a fore-arc basin separating the arc from a continental landmass to the north (Fig. 2). Because Abu Marwat and Hadrabiya BIFs have granular to pisolitic textures (Fig. 3e and g; Essawy et al., 1997), they were likely formed in a shallow marine environment, most likely along the margin of the continental land mass to the north of the fore arc basin (present day coordinates). This model of BIF deposition in northern and southern basins separated by an island arc would explain the chemical differences between the various BIFs (Supplementary Fig. 3a and b), as well as the different directions of fold vergence observed in the southern terranes compared to those of the northern deposits (cf. El-Shazly and Khalil, 2016).

6.5. Tectonic evolution of the Central Eastern Desert

The geochemical data presented above for the BIF and host volcanic and volcaniclastic rocks suggest that the CED BIFs formed in different basins associated with a relatively immature oceanic island arc. These results are therefore consistent with the tectonic model of El-Shazly and Khalil (2016). According to this model, the CED BIFs were deposited over a protracted time period 850–700 Ma by hydrothermal activity from submarine vents (e.g. Kato et al., 2006; Thurston et al., 2012) in the fore-, back-, and intra-arc basins of an immature island arc, or from fluids released from the dehydrating fractured subducted slab (e.g. Castro, 1994) in the fore-arc basin. Although the REY patterns of all BIFs are consistent with a low T (< 230 °C) hydrothermal origin, most geochemical data indicate that these BIFs were strongly influenced by seawater (e.g. Fig. 11a; Supplementary Fig. 3c and d). This makes it equally plausible for an origin by high T hydrothermal fluids diluted by seawater. The BIFs of Um Nar, Gebel El Hadid, and Um Ghamis were deposited in the back-arc basin progressively in that order away from their submarine hydrothermal vent. Larger northern BIFs were likely deposited in a fore-arc basin (e.g. Wadi Kareim), with deposits like Abu Marwat and Hadrabiya forming in a shallow marine environment closest to a continental land mass to the north, whereas smaller deposits like Um Anab and El Imra likely developed in intra-arc basins (Figs. 2 and 12).

During periods of arc activity, (which occurred in three main pulses: 827, 772, and 727 Ma; El-Shazly and Khalil, 2016), pyroclastic material filled these intra-, fore-, and back-arc basins imposing anoxic conditions which either inhibited the growth of photosynthetic organisms (e.g. Beukes and Klein, 1992), or reduced the potential for photochemical reactions (e.g. Morris, 1993). As a result, and with continued hydrothermal activity in these basins, the concentration of dissolved Fe^{2+} increased. During periods of arc quiescence, the recovery of biota (e.g. Beukes and Gutzmer, 2008), or increased photolysis (Morris, 1993), led to the oxidation of Fe^{2+} possibly setting off chemoclinal stratification of the water column, and subsequent precipitation of silica and Fe–oxyhydroxides. Such deposition likely occurred repeatedly over a protracted period of time in small silled, sloped, or terraced basins (Dickinson, 1995), possibly triggered by periodic upwelling of Fe^{2+} rich seawater into more oxidized layers (Fig. 12a; Morris, 1993; Cox et al., 2013).

Continuous precipitation of amorphous silica gels and cyclic precipitation of Fe-oxyhydroxides eventually produced alternating layers of jasper (with its typical “dusty hematite”) and iron ore (magnetite ± hematite; e.g. Beukes and Gutzmer, 2008). Fine-grained magnetite (magnetite I; Fig. 4b) formed diagenetically from the Fe-oxyhydroxides either by dissimilatory Fe reduction or by the addition of more Fe^{2+} supplied from the upwelling hydrothermal fluids into iron – rich sediments (Ohmoto et al., 2006; Beukes and Gutzmer, 2008). The segregation of jasper/ chert bands from the iron ore was likely accomplished by compaction and desiccation. Following the formation of the BIFs, many deposits were locally affected by hydrothermal

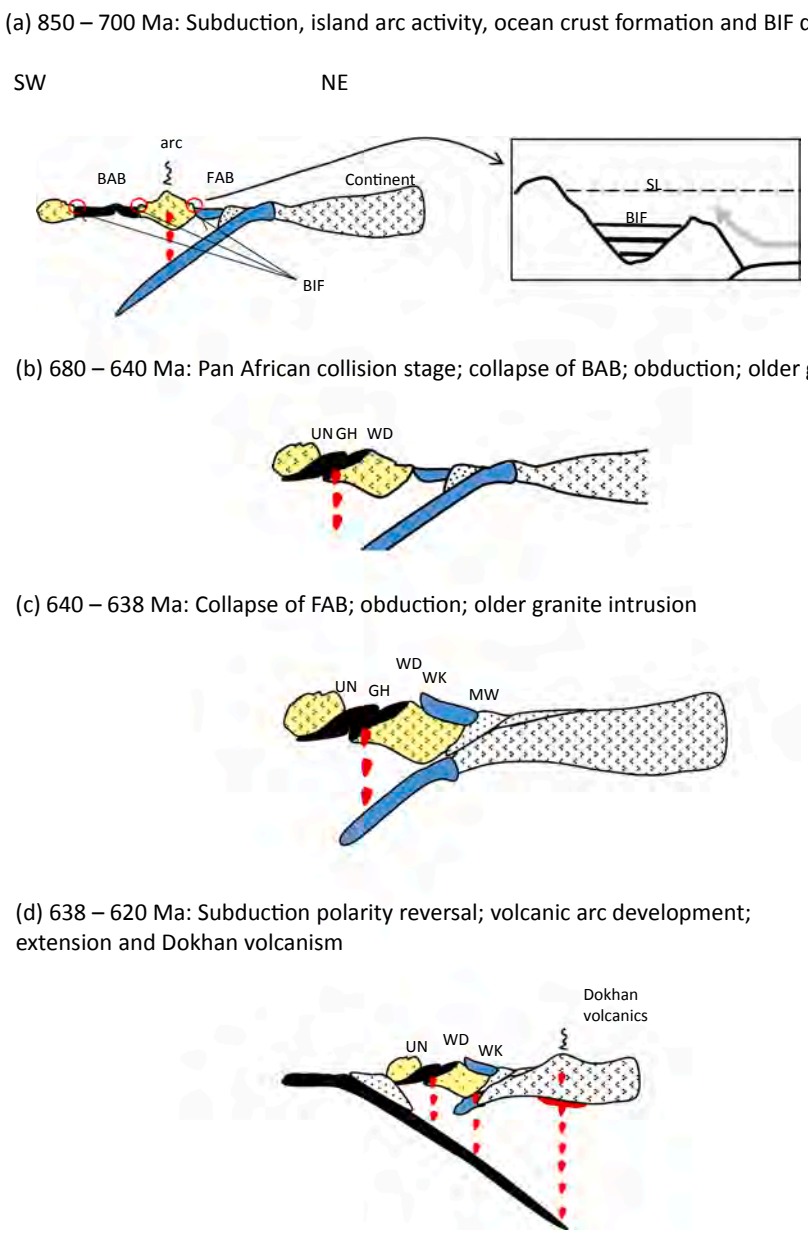

Fig. 12. Proposed tectonic evolution for CED depicted through several cross sectional views all in the NE–SW direction (present day coordinates) Red circles: possible locations for the deposition of BIFs. Inset for Fig. (a) shows the proposed depositional model for BIF in a silled terraced fore- or back- arc basin (cf. Dickinson, 1995); SL: sea level; arrow represents upwelling of relatively anoxic waters into the oxygenated silled basin. BAB: back-arc basin, FAB: fore-arc basin, UN, GH, WD, WK, and MW: relative locations of BIFs of Um Nar, Gebel El Hadid, Wadi El Dabbah, Wadi Kareim, and Abu Marwat, respectively. (For interpretation of the references to colour in this figure legend, the reader is referred to the web version of this article.)

alteration while on the ocean floor (and after their emplacement on the arc), resulting in the local recrystallization of magnetite II (Fig. 3c–f). The source of these hydrothermal fluids remains uncertain, although serpentinization of ultramafic rocks (El-Shazly and Khalil, 2016), or intrusion of syn- to post-collisional acidic magmas are possible driving mechanisms.

Continued convergence coupled with increased compressional forces exerted on the back-arc basin led to intra-oceanic detachment, generation of an ophiolitic mass, and inception of the collisional stage of the Pan African Orogeny *c.* 690–680 Ma (Fig. 12b). During this stage, the BIFs, volcaniclastics, and parts of the oceanic crust and lithospheric mantle in the back arc basin were all thrust northward onto the island arc, producing the north to northeast/ east–verging folds and numerous ophiolitic thrust sheets observed in Um Nar, Gebel El Hadid, Um Ghamis and Wadi El Dabbah (Figs. 1, 2 and 12b). Thrust sheet stacking resulted in regional metamorphism of the allochthonous "ophiolitic melange and arc assemblage" under epidote amphibolite to greenschist facies conditions (El-Shazly and Khalil, 2016), which led to the formation of coarse-grained magnetite (magnetite III, Fig. 3g) and specular hematite (Fig. 3i) by recrystallization of magnetite I and II. Oxygen fugacity conditions during regional metamorphism were controlled by the hematite – magnetite buffer (El-Shazly and Khalil, 2014). This stage was also accompanied by the intrusion of the "Older granites" which are syncollisional to post-orogenic metaluminous I-type granitoids (Backus et al., 2012), and may have contributed to hydrothermal alteration of some BIFs.

Continued subduction and obduction eventually led to the closure of the fore-arc basin, and the subsequent emplacement of the northern ophiolitic bodies to the south onto the former island arc *c.* 640 Ma (Fig. 12c). This process produced the SW–verging folds and thrusts observed in Wadi Kareim and Abu Marwat, and open type folding in Um Nar, Gebel El Hadid, Um Ghamis, and Wadi El Dabbah to the south (D3 transpression; Fig. 2), accompanied by greenschist facies regional metamorphism (El-Shazly and Khalil, 2016). The collapse of the fore- and back-arc basins and the attempted subduction of part of the continental landmass resulted in the reversal of the subduction polarity and the development of a new trench to the south of all thrust stacks (Fig. 12d). Subduction along a N–dipping zone resulted in continued intrusion of I-type syntectonic granitoids in pulses *c.* 640–620 Ma as indicated by zircon ages (e.g. Moussa et al., 2008; Backus et al., 2012;

El-Shazly and Khalil, 2016). North-directed subduction beneath thrust stacks of the "ophiolitic melange – arc assemblage" and the continental landmass also led to magmatic activity manifested by Dokhan volcanics (Fig. 12d) which are restricted to the NED (Figs. 1 and 2). This stage was followed by several stages of shearing and strike-slip faulting related to the Najd System (D4; Fig. 2; Loizenbauer et al., 2001), and the intrusion of post-tectonic anorogenic "Younger granites" *c.* 620–505 Ma (e.g. Hassan and Hashad, 1990).

7. Conclusions

The geochemical results of CED BIFs and their host rocks lead us to the following conclusions:

- All BIFs have a hydrogenous origin influenced by hydrothermal solutions, and received a relatively small amount of detrital material.
- Both Fe and Si were provided by submarine hydrothermal solutions on the floors of small, isolated basins adjacent to an active, relatively immature, island arc.
- Although the CED BIFs are Neoproterozoic in age, they are non-glaciogenic in origin. BIF mineral precursors were precipitated during periods of arc quiescence, triggered by upwelling of Fe^{2+} rich hydrothermal fluids into more oxygenated layers of small, terraced or sloped, silled basins in the fore- and back-arc areas, or in intra-arc basins.
- Geochemical trends, Y/Ho, and Pr/Yb ratios suggest that Wadi El Dabbah BIF was deposited closest to the arc, whereas Um Nar, Gebel El Hadid, and Abu Marwat formed farthest from it. Small deposits such as El Imra and Um Anab characterized by a higher detrital component likely formed in intra-arc basins.
- Geochemical correlations and factor analysis show 4 to 5 main factors the most prominent of which are the positively correlated Al, Mg, Y, ± Zr ± Ti factor representing detrital components, and the Fe and Si ± Cu factor representing the chemical precipitates. Correlation diagrams among the detrital factor elements show three distinct trends, which may reflect three main volcanic pulses from the active island arc.
- Hydrothermal alteration manifested by secondary Ca-rich minerals was localized and may have been related to either serpentinization of ultrabasic bodies, or intrusion of older granitoids. However, the geochemical data presented is insufficient to support either conclusion.
- Weathering had a variable effect on different BIF samples, but increased their Fe^{3+}/Fe^{2+} ratios and generally leached silica increasing some of their trace element concentrations.
- The geochemical data provided for the two samples from El Imra, which suggest an intra-arc origin, are relatively enigmatic (very high Ca, Al, Y, V, Sc, La, and Ce) compared to the other BIFs. More work on a larger number of samples from this area is therefore needed.

Acknowledgements

The authors thank Ethan Backus, Nathan Rohrbaugh, Kelli Gagnon, and Patrick Foster for assistance with sample processing/ analysis, and Magdy Moheb for thin/ polished section preparation. Discussions with A. Maurice and A. Al-Khiamy in the field were very helpful. AES thanks Dr. M. Ismail Abdelkareem of South Valley University, Egypt, for sharing his yet unpublished data on Abu Marwat with us. KIK expresses his gratitude to B. Lehmann of Technical University of Clausthal, Germany, for hosting and mentoring him while working on Gebel El Hadid samples. Detailed reviews by two anonymous reviewers, and editorial handling by Dr. Kamal Ali have greatly improved this paper. Any remaining errors are the sole responsibility of the authors. This project was funded by NSF OISE 1004021 to AES.

Appendix A. Supplementary data

Supplementary data to this article can be found online at https://doi.org/10.1016/j.precamres.2019.02.011.

References

Abbott, D., Isley, A., 2001. Oceanic upwelling and mantle plume activity: Paleomagnetic tests of ideas on the source of the Fe in early Precambrian iron formations. In: Ernst, R.E., Buchan, K.L. (Eds.), Mantle plumes: their identification through time. Special Paper 352. Geological Society of America, Boulder, Colorado, USA, pp. 323–339.

Abd El-Rahman, Y.A., Polat, A., Dilek, Y., Fryer, B.J., El-Sharkawy, M., Sakran, S., 2009. Geochemistry and tectonic evolution of the Neoproterozoic incipient arc–forearc crust in the Fawakhir area, Central Eastern Desert of Egypt. Precambr. Res. 175, 116–134.

Agrawal, S., Guevara, M., Verma, S.P., 2008. Tectonic discrimination of basic and ultrabasic volcanic rocks through log-transformed ratios of immobile trace elements. Int. Geol. Rev. 50 (12), 1057–1079.

Aitchison, J., 1986. The Statistical Analysis of Compositional Data. Chapman and Hall, London, pp. 417.

Ali, K.A., Stern, R.J., Manton, W.I., Kimura, J.-I., Khamees, H.A., 2009. Geochemistry, Nd isotopes and U-Pb SHRIMP zircon dating of Neoproterozoic volcanic rocks from the Central Eastern Desert of Egypt: New insights into the ~750 Ma crust-forming event. Precambr. Res. 171, 1–22.

Ali, K.A., Stern, R.J., Manton, W.I., Johnson, P.R., Mukherjee, S.K., 2010. Neoproterozoic diamictite in the Eastern Desert of Egypt and Northern Saudi Arabia: evidence of ~750 Ma glaciation in the Arabian-Nubian Shield? Int. J. Earth Sci. 99, 705–726.

Andresen, A., El-Rus, M.A.A., Myhre, P.I., Boghdady, G.Y., Corfu, F., 2007. U-Pb TIMS age constraints on the evolution of the Neoproterozoic Meatiq Gneiss Dome, Eastern Desert, Egypt. Int. J. Earth Sci. 98, 481–497.

Backus, E.L., Gagnon, K.E., El-Shazly, A.K., Khalil, K.I., 2012. Geochemistry of the Banded Iron Formations and their host rocks, Eastern Desert of Egypt. Geol. Soc. Am. Abstr. Programs 44 (7), 245.

Basta, F.F., Maurice, A.E., Fontboté, L., Favarger, P.-Y., 2011. Petrology and geochemistry of the banded iron formation (BIF) of Wadi Karim and Um Anab, Eastern Desert, Egypt: implications for the origin of Neoproterozoic BIF. Precambr. Res. 187 (3–4), 277–292.

Bau, M., Dulski, P., 1996. Distribution of yttrium and rare-earth elements in the Penge and Kuruman iron-formations, Transvaal Supergroup, South Africa. Precambr. Res. 79 (1–2), 37–55.

Bau, M., Dulski, P., 1999. Comparing ytrium and rare earths in hydrothermal fluids from the Mid-Atlantic Ridge: implications for Y and REE behaviour during nearvent mixing and for the Y/Ho ratio of Proterozoic seawater. Chem. Geol. 155, 77–90.

Bekker, A., Slack, J.F., Planavsky, N., Krapez, B., Hofmann, A., Konhauser, K.O., Rouxel, O.J., 2010. Iron Formation: the Sedimentary Product of a Complex Interplay among Mantle, Tectonic, Oceanic, and Biospheric Processes. Econ. Geol. 105, 467–508.

Beukes, N.J., Gutzmer, J., 2008. Origin and paleoenvironmental significance of major iron formations at the Archean-Paleoproterozoic boundary. Revi. Econ. Geol. 15, 5–47.

Beukes, N.J., Klein, C., 1992. Models for iron formation deposition. In: Schopf, J.W., Klein, C. (Eds.), The Proterozoic Biosphere: A Multidisciplinary Study. Cambridge University Press, New York, pp. 147–151.

Bhatia, M.R., 1983. Plate tectonics and geochemical composition of sandstones. J. Geol. 91 (6), 611–627.

Bhatia, M.R., Crook, K.A., 1986. Trace element characteristics of graywackes and tectonic setting discrimination of sedimentary basins. Contrib. Miner. Petrol. 92 (2), 181–193.

Blatt, H., Middleton, G., Murray, R., 1980. Origin of Sedimentary Rocks. Prentice Hall, New Jersey.

Huston, D.L., Logan, G.A., 2004. Barite, BIFs and bugs: evidence for the evolution of the Earth's early hydrosphere. Earth Planet. Sci. Lett. 220, 41–55.

Breitkreuz, C., Eliwa, H., Khalaf, I., Gameel, K.E., Bühler, B., Sergeev, S., Larionov, A., Murata, M., 2010. Neoproterozoic SHRIMP U-Pb zircon ages of silica-rich Dokhan volcanics in the North Eastern Desert, Egypt. Precambr. Res. 182, 163–174.

Briggs, P. H., 2002. Determination of 27 elements in aqueous samples by inductively coupled plasma atomic emission spectroscopy. USGS open file report 02-0223.

Cabanis, B., Lecolle, M., 1989. Le diagramme La/10-Y/15-Nb/8: un outil pour la discimination des series volcaniques et la mise en evidence des processus de melange et/ou de contamination crustale. C. R. Acad. Sci. Ser. IIA 309, 2023–2029.

Castro, L.O., 1994. Genesis of banded iron-formations. Econ. Geol. 89, 1384–1397.

Cox, G.M., Halverson, G.P., Minarik, W.G., Le Heron, D.P., Macdonald, F.A., Bellefroid, E.J., Strauss, J.V., 2013. Neoproterozoic iron formation: an evaluation of its temporal, environmental and tectonic significance. Chem. Geol. 362, 232–249.

Cremer, M., Schlocker, J., 1976. Lithium borate decomposition of rocks, minerals, and ores. Am. Mineral. 61, 318–321.

Delijska, A., Blazheva, T., Petkova, L., Dimov, L., 1988. Fusion with lithium borate as sample preparation for ICP and AAS analysis. Fresenius' Z. Anal. Chem. 332 (4), 362–365.

Derry, L.A., Jacobsen, S.B., 1990. The chemical evolution of Precambrian seawater: evidence from REEs in banded iron formations. Geochim. Cosmochim. Acta 54, 2965–2977.

Dickinson, W.R., 1995. Forearc basins. In: Busby, C., Ingersoll, R.V. (Eds.), Tectonics of Sedimentary Basins. Blackwell, Oxford, pp. 221–261.

Egyptian Geological Survey 1981. Geological Map of Egypt. Accessed 2010-09-03 at http://library.wur.nl/isric/kaart/origineel/afr_egg.jpg. June, 2018.

El Aref, M.M., El Doudgdoug, A., Abdel Wahed, M., El Manawi, A.W., 1993. Diagenetic and metamorphic history of Umm Nar BIF, Eastern Desertm Egypt. Miner. Deposita 28, 264–278.
El Habaak, G.H., 2004. Pan-African skarn deposits related to banded iron formation, Um Nar area, central Eastern Desert, Egypt. J. Afr. Earth Sci. 38 (2), 199–221.
El-Gaby, S., List, F.K., Tehrani, R., 1990. The basement complex of the Eastern Desert and Sinai. In: Said, R. (Ed.), The Geology of Egypt. Balkema, Rotterdam, pp. 175–184.
El-Nisr, S.A., 1997. Late Precambrian volcanism at Wadi Allaqi, south Eastern Desert, Egypt: evidence for transitional continental arc/margin environment. J. Afr. Earth Sci. 24, 301–313.
El-Sayed, M.M., Obeid, M.A., Furnes, H., Moghazi, A.M., 2004. Late Neoproterozoic volcanism in the southern Eastern Desert, Egypt: petrological, structural and geochemical constraints on the tectonic-magmatic evolution of the Allaqi Dokhan volcanic suite Neues Jahrbuch für Mineralogie-Abhandlungen. J. Mineral. Geochem. 180, 261–286.
El-Shazly, A.K., Khalil, K.I., Rohrbaugh, N., Gagnon, K., 2011. Multi-stage origin of Neoproterozoic banded iron formations from Egypt. Abstract B41F-0263, Fall Meeting. American Geophysical Union.
El-Shazly, A., Khalil, K., 2014. Banded iron formations of Um Nar, Eastern Desert of Egypt: P-T–X conditions of metamorphism and tectonic implications. Lithos 196, 356–375.
El-Shazly, A.K., Khalil, K.I., 2016. Metamorphic and Geochronologic constraints on the tectonic evolution of the Central Eastern Desert of Egypt: implications for origin of some Neoproterozoic Banded Iron Formations. Precambr. Res. 283, 144–168. https://doi.org/10.1016/j.precamres.2016.07.016.
Essawy, M.A., Zalata, A.A., Makroum, F., 1997. Hadrabia banded iron-formation, Eastern Desert, Egypt. Egypt. Mineral. 9, 147–168.
Eyles, N., Januszczak, N., 2004. 'Zipper-rift': a tectonic model for Neoproterozoic glaciations during the breakup of Rodinia after 750 Ma. Earth Sci. Rev. 65 (1), 1–73.
Farahat, E., 2010. Neoproterozoic arc–back-arc system in the Central Eastern Desert of Egypt: evidence from supra-subduction zone ophiolites. Lithos 120 (3), 293–308.
Floyd, P.A., Winchester, J.A., 1975. Magma type and tectonic setting discrimination using immobile elements. Earth Planet. Sci. Lett. 27 (2), 211–218.
Floyd, P.A., Winchester, J.A., 1978. Identification and discrimination of altered and metamorphosed volcanic rocks using immobile elements. Chem. Geol. 21 (3–4), 291–306.
Floyd, P.A., Winchester, J.A., Park, R.G., 1989. Geochemistry and tectonic setting of Lewisian clastic metasediments from the Early Proterozoic Loch Maree Group of Gairloch, NW Scotland. Precambr. Res. 45 (1–3), 203–214.
Freitas, B.T., Warren, L.V., Boggiani, P.C., De Almeida, R.P., Piacentini, T., 2011. Tectono-sedimentary evolution of the Neoproterozoic BIF-bearing Jacadigo Group, SW-Brazil. Sediment. Geol. 238 (1), 48–70.
Fritz, S.F., Popp, R.K., 1985. A single-dissolution technique for determining FeO and Fe 2 O 3 in rock and mineral samples. Am. Mineral. 70 (9–10), 961–968.
Fryer, B.J., 1977. Rare earth evidence in iron-formations for changing Precambrian oxidation states. Geochim. Cosmochim. Acta 41, 361–367.
Fryer, B.J., 1983. Part B. Rare Earth Elements in Iron-formation. In Developments in Precambrian Geology 6:, 345–358.
Garrels, R.M., Perry Jr., E.A., McKenzie, F.T., 1973. Genesis of Precambrian iron formations and the development of atmospheric oxygen. Econ. Geol. 68, 1173–1179.
Graf Jr., J.L., 1978. Rare earth elements, iron formations and sea water. Geochim. Cosmochim. Acta 42, 1845–1850.
Gross, G.A., 1996. Algoma-type Iron-formation. In: Lefebure, D.V., Hoy, T. (Eds.), Selected British Columbia Mineral Deposit Profiles, Volume 2 – Metallic Deposits. British Columbia Ministry of Employment and Investment, Open File 1996-13, pp. 25–28.
Gross, G.A., McLeod, C.R., 1980. A preliminary assessment of the chemical composition of iron formations in Canada. Can Mineral. 18 (2), 223–229.
Hamimi, Z.E., 1988. Geology and structure of Gebel El Hadid area, Eastern Desert. M.Sc. Thesis. Thesis, Zagazig University, Egypt, pp. 108.
Harman, H.H., 1976. Modern Factor Analysis. University of Chicago Press, pp. 486 pp..
Hassan, M., Hashad, A., 1990. Precambrian of Egypt. In: The Geology of Egypt. Brookfield, Balkema, Rotterdam, pp. 201–245.
Hawkesworth, C.J., Gallagher, K., Hergt, J.M., McDermott, F., 1993a. Mantle and slab contributions in arc magmas. Annu. Rev. Earth Planet. Sci. 21 (1), 175–204.
Hawkesworth, C.J., Gallagher, K., Hergt, J.M., McDermott, F., 1993b. Trace element fractionation processes in the generation of island arc basalts. Phil. Trans. R. Soc. Lond. A 342, 179–191.
Hoffman, P.F., Kaufman, A.J., Halverson, G.P., Schrag, D.P., 1998. A Neoproterozoic snowball earth. Science 281 (5381), 1342–1346.
Hollocher, K., Robinson, P., Walsh, E., Roberts, D., 2012. Geochemistry of amphibolite-facies volcanics and gabbros of the Støren Nappe in extensions west and southwest of Trondheim, Western Gneiss Region, Norway: a key to correlations and paleotectonic settings. Am. J. Sci. 312, 357–416.
Ilyin, A.V., 2009. Neoproterozoic banded iron formations. Lithol. Min. Resour. 44 (1), 78–86.
Ingamells, C.O., 1966. Absorptiometric methods in rapid silicate analysis. Anal. Chem. 38, 1228–1234.
Isley, A.E., 1995. Hydrothermal plumes and the delivery of iron to banded iron formation. J. Geol. 103 (2), 169–185.
Isley, A.E., Abbott, D.H., 1999. Plume-related mafic volcanism and the deposition of banded iron-formation. J. Geophys. Res. 104, 15461–15477.
Developments in Sedimentology, vol. 7, 543–589.
Kaiser, H.F., 1960. The application of electronic computers to factor analysis. Educ. Psychol. Measur. 20 (1), 141–151.
Kato, Y., Yamaguchi, K.E., Ohmoto, H., 2006. Rare earth elements in Precambrian banded iron formations: secular changes of Ce and Eu anomalies and evolution of atmospheric oxygen. Geol. Soc. Am. Memoirs 198, 269–289.
Khalil, K., El-Shazly, A., 2012. Petrological and geochemical characteristics of Egyptian banded iron formations: review and new data from Wadi Kareim. Geochem. Explor. Environ. Anal. 12 (2), 105–126.
Khalil, K.I., El-Shazly, A.K., Lehmann, B., 2015. Late Neoproterozoic banded iron formation (BIF) in the central Eastern Desert of Egypt: mineralogical and geochemical implications for the origin of the Gebel El Hadid iron ore deposit. Ore Geol. Rev. 69, 380–399.
Kirschvink, J.L., 1992. Late Proterozoic low-latitude global glaciation: the snowball Earth.
Klein, C., 2005b. Some Precambrian banded iron-formations (BIFs) from around the world: Their age, geologic setting, mineralogy, metamorphism, geochemistry, and origins. Am. Mineral. 90 (10), 1473–1499.
Klein, C., 2005a. Some Precambrian banded iron formations from around the world: their age, geologic setting, mineralogy, metamorphism, geochemistry, and origin. Am. Mineral. 90, 1473–1499.
Klein, C., Beukes, N.J., 1993b. Sedimentology and geochemistry of late Proterozoic Rapitan iron formation in Canada. Econ. Geol. 88, 542–565.
Klein, C., Beukes, N.J., 1993a. Proterozoic iron-formations. In: Condie, K.C. (Ed.), Development in Precambrian Geology: Proterozoic Crustal Evolution, pp. 383–418.
Klein, C., Ladeira, E.A., 2004. Geochemistry and mineralogy of Neoproterozoic banded iron-formations and some selected siliceous manganese formations from the Urucum District, Matto Grosso do Sul, Brazil. Econ. Geol. 99, 1233–1244.
Kröner, A., Stern, R.J., 2004. In: Pan-African Orogeny. Encyclopedia of Geology, pp. 1–12.
Le Bas, M.L., Maitre, R.L., Streckeisen, A., Zanettin, B., 1986. IUGS Subcommission on the Systematics of Igneous Rocks, 1986. A chemical classification of volcanic rocks based on the total alkali-silica diagram. J. Petrol. 27 (3), 745–750.
Li, C., Arndt, N.T., Tang, Q., Ripley, E.M., 2015. Trace element indiscrimination diagrams. Lithos 232, 76–83.
Lobato, L.M., Figueiredo e Silva, R.C., Hagemann, S.G., Thorne, W.S., Zuchetti, M., 2008. Hypogene alteration associated with high-grade banded iron formation-related iron ore. Econ. Geol. (SEG Reviews) 15, 107–128.
Loizenbauer, J., Wallbrecher, E., Fritz, H., Neumayr, P., Khudeir, A., Kloetzli, U., 2001. Structural Geology, single zircon ages and fluid inclusion studies of the Meatiq metamorphic core complex: Implications for Neoproterozoic tectonics in the Eastern Desert of Egypt. Precambr. Res. 110 (1), 357–383.
Meschede, M., 1986. A method of discriminating between different types of mid-ocean ridge basalts and continental tholeiites with the Nb 1bZr 1bY diagram. Chem. Geol. 56 (3–4), 207–218.
Morris, R., 1993. Genetic modelling for banded iron-formation of the Hamersley Group, Pilbara Craton, Western Australia. Precambr. Res. 60, 243–286.
Moussa, E.M.M., Stern, R.J., Manton, W.I., Ali, K.A., 2008. SHRIMP zircon dating and Sm/Nd isotopic investigations of Neoproterozoic granitoids, Eastern Desert, Egypt. Precambr. Res. 160, 341–356.
Nance, W.B., Taylor, S.R., 1976. Rare earth element patterns and crustal evolution—I. Australian post-Archean sedimentary rocks. Geochim. Cosmochim. Acta 40, 1539–1551.
Noweir, M.A., Ghoneim, M.F., Abu Alam, T.S., 2004. Structural framework and geochemical studies of iron-ore deposits of Wadi Kareim, Central Eastern Desert. In: 6th International Conference on Geochemistry. Alexandria University, Egypt, I-B, pp. 821–847.
Ohmoto, H., Watanabe, Y., Yamaguchi, K.E., Naraoka, H., Haruna, M., Kakegawa, T., Hayashi, K.I., Kato, Y., 2006. Chemical and biological evolution of early Earth: constraints from banded iron formations. Geol. Soc. Am. Mem. 198, 291–331.
Pearce, J.A., 1982. Trace element characteristics of lavas from destructive plate boundaries. In: Orogenic Andesites and Related Rocks, pp. 528–548.
Pearce, J.A., 2008. Geochemical fingerprinting of oceanic basalts with applications to ophiolite classification and the search for Archean oceanic crust. Lithos 100 (1–4), 14–48.
Pearce, J.A., 2014. Immobile element fingerprinting of ophiolites. Elements 10 (2), 101–108.
Pearce, J.A., Cann, J.R., 1973. Tectonic setting of basic volcanic rocks determined using trace element analyses. Earth Planet. Sci. Lett. 19 (2), 290–300.
Pearce, J.A., Norry, M.J., 1979. Petrogenetic implications of Ti, Zr, Y, and Nb variations in volcanic rocks. Contrib. Miner. Petrol. 69 (1), 33–47.
Peccerillo, A., Taylor, S.R., 1976. Geochemistry of Eocene calc-alkaline volcanic rocks from the Kastamonu area, northern Turkey. Contrib. Miner. Petrol. 58 (1), 63–81.
Peres-Neto, P.R., Jackson, D.A., Somers, K.M., 2003. Giving meaningful interpretation to ordination axes: assessing loading significance in principal component analysis. Ecology 84 (9), 2347–2363.
Peter, J.M., 2003. Ancient iron formations: their genesis and use in the exploration for stratiform base metal sulfide deposits, with examples from the Bathurst Mining Camp. In: Lentz, D.R. (Ed.), Geochemistry of Sediments and Sedimentary Rocks: Evolution Considerations to Mineral Deposit-Forming Environments. Geological Association of Canada, GeoText 4, pp. 145–176.
Pettijohn, F.J., Potter, P.E., Siever, R., 1973. Sand and Sandstone, 618 pp. New York/Heidelberg/Berlin.
Roser, B.P., Korsch, R.J., 1988. Provenance signatures of sandstone-mudstone suites determined using discriminant function analysis of major-element data. Chem. Geol. 67 (1–2), 119–139.
Salem, A.K., Niazy, E.A., Kamel, O.A., 1994. New occurrence of contact metasomatic iron ores in El Imra area, Eastern Desert, Egypt: its mineralogy and origin. Egypt. Mineral. 6, 53–75.
Schmidt, K., Garbe-Schoenberg, D., Koschinsky, A., Strauss, H., Jost, C.I., Klevenz, V.,

Koeniger, P., 2011. Fluid elemental and stable isotope composition of the Nibelungen hydrothermal field: Constraints on fluid-rock interaction in heterogenous lithosphere. Chem. Geol. 280, 1–18.
Shalaby, A., Stuwe, K., Makroum, F., Fritz, H., Kebede, T., Klotzli, U., 2005. The Wadi Mubarak belt, Eastern Desert of Egypt: a Neoproterozoic conjugate shear system in the Arabian? Nubian Shield. Precambr. Res. 136, 27–50.
Shapiro, L., 1975. Rapid analysis of silicate, carbonate and phosphate rocks, revised edition. In: United States Geological Survey Bulletin, pp. 1–54.
Shervais, J.W., 1982. Ti-V plots and the petrogenesis of modern and ophiolitic lavas. Earth Planet. Sci. Lett. 59 (1), 101–118.
Simonson, B.M., 2003. Origin and evolution of large Precambrian iron formations. In: Chan, M.A., Archer, A.W. (Eds.), Extreme depositional environments: Mega end members in geological time. Geological Society of America Special Paper 370, Boulder, Colorado, USA, pp. 231–244.
Sims, P.K., James, H.L., 1984. Banded iron ore formation of Late Proterozoic age in the Central Eastern Desert, Egypt: geological and tectonic setting. Econ. Geol. 79, 1777–1784.
Stern, R.J., Gottfried, D., Hedge, C.E., 1984. Late Precambrian rifting and crustal evolution in the Northeastern Desert of Egypt. Geology 12, 168–172.
Stern, R.J., Hedge, C.E., 1985. Geochronologic and isotopic constraints on Late Precambrian crustal evolution in the Eastern Desert of Egypt. Am. J. Sci. 285, 97–127.
Stern, R.J., Mukherjee, S., Miller, N.R., 2013. ~750 Ma banded iron formation from the arabian-nubian shield – implications for understanding Neoproterozoic tectonics, volcanism, and climate change. Precambr. Res. 239, 79–94.
Suhr, N.H., Ingamells, C.O., 1966. Solution Technique for analysis of silicates. Anal. Chem. 38, 730.
Sun, S.S., McDonough, W.S., 1989. Chemical and isotopic systematics of oceanic basalts: implications for mantle composition and processes. In: Geological Society, London, Special Publications, pp. 313–345.
Takla, M.A., Hamimi, Z., Hassanein, S.M., Kaoud, N.N., 1999. Characterization and genesis of the BIF associating arc metavolcanics, Umm Ghamis area, Central Eastern Desert Egypt. Egypt. Mineral. 11, 157–185.
Thurston, P.C., Kamber, B.S., Whitehouse, M., 2012. Archean cherts in banded iron formation: insight into Neoarchean ocean chemistry and depositional processes. Precambr. Res. 214, 227–257.
Whitney, D.L., Evans, B.W., 2010. Abbreviations for names of rock-forming minerals. Am. Mineral. 95, 185.
Wonder, J., Spry, P., Windom, K., 1988. Geochemistry and origin of manganese-rich rocks related to iron-formation and sulfide deposits, western Georgia. Econ. Geol. 83, 1070–1081.
Yeo, G.M., 1986. . Iron-formation in the Late Proterozoic Rapitian Group, Yukon and Northwest Territories. In: Morin, J.A. (Ed.), Mineral Deposits of the Northern Cordillera. Canadian Institute of Mineralogy and Metallurgy Special Volume, pp. 142–153.
Zhang, J., Nozaki, Y., 1996. Rare earth elements and yttrium in seawater: ICP-MS determinations in the East Caroline, Coral Sea, and South Fiji basins of the western South Pacific Ocean. Geochim. Cosmochim. Acta 60 (23), 4631–4644.